

1 **Holocene climates of the Iberian Peninsula: pollen-based reconstructions of changes in**  
2 **the west-east gradient of temperature and moisture**

3 Mengmeng Liu<sup>1\*</sup>, Yicheng Shen<sup>2</sup>, Penelope González-Sampériz<sup>3</sup>, Graciela Gil-Romera<sup>3</sup>,  
4 Cajo J. F. ter Braak<sup>4</sup>, Iain Colin Prentice<sup>1</sup>, Sandy P. Harrison<sup>2</sup>

5 1: Department of Life Sciences, Imperial College London, Silwood Park Campus, Buckhurst  
6 Road, Ascot SL5 7PY, UK

7 2: Geography & Environmental Science, Reading University, Whiteknights, Reading, RG6  
8 6AH, UK

9 3: Instituto Pirenaico de Ecología-CSIC, Avda. Montaña 1005, 50059, Zaragoza, Spain

10 4: Biometris (Applied Mathematics and Applied Statistics Centre), Wageningen University &  
11 Research, 6708 PB Wageningen, The Netherlands

12 \*: Corresponding author: Mengmeng Liu (m.liu18@imperial.ac.uk)

13 Ms for: *Climate of the Past*

14 **Abstract**

15 The Iberian Peninsula is characterised by a steep west-east moisture gradient today, reflecting  
16 the dominance of maritime influences along the Atlantic coast and more Mediterranean-type  
17 climate further east. Holocene pollen records from the Peninsula suggest that this gradient was  
18 less steep during the mid-Holocene, possibly reflecting the impact of orbital changes on  
19 circulation and thus regional patterns in climate. Here we use 7214 pollen samples from 117  
20 sites covering part or all of the last 12,000 years to reconstruct changes in seasonal temperature  
21 and in moisture across the Iberian Peninsula quantitatively. We show that there is an increasing  
22 trend in winter temperature at a regional scale, consistent with known changes in winter  
23 insolation. However, summer temperatures do not show the decreasing trend through the  
24 Holocene that would be expected if they were a direct response to insolation forcing. We show  
25 that summer temperature is strongly correlated with plant-available moisture ( $\alpha$ ), as measured  
26 by the ratio of actual evapotranspiration to equilibrium evapotranspiration, which declines  
27 through the Holocene. The reconstructions also confirm that the west-east gradient in moisture  
28 was considerably less steep than today during the mid-Holocene, indicating that atmospheric  
29 circulation changes (possibly driven by orbital changes) have been important determinants of  
30 the Holocene climate of the region.

31 **1. Introduction**

32 The Iberian Peninsula is characterised by a steep west-east gradient in temperature and  
33 moisture today, reflecting the dominance of maritime influences along the Atlantic coast and  
34 more Mediterranean-type climate further east. Projections of future climate change suggest that  
35 the region will become both warmer and drier, but nevertheless show that this west-east  
36 differentiation is maintained (Andrade et al., 2021a). The changes in temperature are projected  
37 to be larger and the occurrence of extreme temperature episodes more frequent in the south-  
38 central and eastern parts of Iberia than in Atlantic coastal areas (Carvalho et al., 2021). Similar  
39 gradients are seen in future projections of precipitation change, with largest reductions in  
40 precipitation in the south-central region (Andrade et al., 2021b). However, the stability of these  
41 west-east gradients during the Holocene has been questioned. In particular, the west-east  
42 gradient in moisture appears to have been less pronounced during the mid-Holocene (8~4 ka)  
43 when cooler summers and wetter conditions in the Atlantic zone (e.g. Martínez-Cortizas et al.,  
44 2009; Mauri et al., 2015) coincided with the maximum development of mesophytic vegetation  
45 further east and south (Aranbarri et al., 2014, 2015; Carrión et al., 2010, 2009; González-  
46 Sampériz et al., 2017).

47 However, much of the evidence for Holocene climates of the Iberian Peninsula is based on  
48 qualitative interpretations of vegetation changes, generally interpreted as reflecting changes in  
49 moisture availability (Morellón et al., 2018; Ramos-Román et al., 2018; Schröder et al., 2019).  
50 These records are extensive and they seem to indicate fairly complex spatial patterns of change.  
51 Kaufman et al. (2020) provides quantitative reconstructions of summer and winter temperature  
52 in their compilation of Holocene climate information, but there are only 5 terrestrial sites from  
53 the Iberian Peninsula. Iberia was also included in the quantitative pollen-based reconstructions  
54 of European climate through the Holocene in Mauri et al. (2015), which is an update of Davis  
55 et al. (2003). However, the geographical distribution of sites included is uneven and a large  
56 fraction of the records were from the Pyrenees and the Cantabrian mountains, with additional  
57 clustering of sites in coastal regions. Thus, the inferred patterns of climate over most of the  
58 central part of the Peninsula are therefore largely extrapolated. Tarroso et al. (2016) has  
59 provided reconstructions of summer and winter temperature and mean annual precipitation  
60 since the Last Glacial Maximum for the Iberian Peninsula, by using modern species distribution  
61 data to develop climate probability distribution functions (PDFs) and applying these to 31 fossil  
62 records. However, although they identified trends in precipitation during the Holocene, the

63 temperature reconstructions do not seem to be reliable since they show no changes through  
64 time (9~3 ka), either for the Iberian Peninsula as a whole or for individual sub-regions, in  
65 contradiction to the other reconstructions. The current state of uncertainty about Holocene  
66 climate changes in Iberia is further exacerbated because quantitative reconstructions of summer  
67 temperature made at individual sites using chironomid data (Muñoz Sobrino et al., 2013;  
68 Tarrats et al., 2018) are not consistent with reconstructed summer temperatures based on pollen  
69 for the same sites.

70 We used the Tolerance-weighted Weighted Average Partial Least-Squares regression with a  
71 sampling frequency correction (fxTWA-PLS) method, introduced by Liu et al. (2020) as an  
72 improvement of the widely used Weighted Average Partial Least-Squares (WAPLS: ter Braak  
73 and Juggins, 1993) method for reconstructing past climates from pollen assemblages. As  
74 presented in detail by Liu et al. (2020), this method is a more complete implementation of the  
75 theory underlying WA-PLS because it takes greater account of the climatic information  
76 provided by taxa with more limited climatic ranges and also applies a sampling frequency  
77 correction to reduce the impact of uneven sampling in the training data set. Liu et al. (2020)  
78 showed that fxTWA-PLS does indeed provide better reconstructions than WA-PLS. Here we  
79 have further modified the algorithm implementing fxTWA-PLS, achieving an additional gain  
80 in performance. In the algorithm published by Liu et al. (2020), sampling frequencies were  
81 extracted from a histogram. In the modified algorithm they are estimated using P-splines  
82 smoothing (Eilers and Marx, 2021), which makes the estimates almost independent of the  
83 chosen bin width (see Appendix A for details). In addition, the modified method applies the  
84 sampling frequency correction at two separate steps – the estimation of optima and tolerances,  
85 and the regression step – a measure intended to produce more stable results. The modified  
86 method produces both improved  $R^2$  values and reduced compression and maximum bias in  
87 reconstructed climate variables (see Table A1 and Figs A1–A2). We will return to this point in  
88 the Discussion.

89 We have used this improved method to reconstruct Holocene climates across Iberia, and re-  
90 examined the trends in summer and winter temperature and plant-available moisture, using a  
91 new and relatively comprehensive compilation of pollen data (Shen et al., 2022) with age  
92 models based on the latest radiocarbon calibration curve (IntCal20: Reimer et al., 2020). We  
93 explicitly test whether there are significant differences in the west-east gradient of moisture  
94 and seasonal temperatures through time. We then analyse the relationships between the

95 changes in the three climate variables and how trends in these variables are related to external  
96 climate forcing. These analyses allow us to investigate whether the west-east gradient in  
97 moisture was less steep during the mid-Holocene and explore what controls the patterns of  
98 climate change across the region.

99 **2. Methods**

100 Multiple techniques have been developed to make quantitative climate reconstructions from  
101 pollen (see reviews in Bartlein et al., 2011; Chevalier et al., 2020; Salonen et al., 2011). Modern  
102 analogue techniques (MAT: Overpeck et al., 1985) tend to produce rapid shifts in reconstructed  
103 values corresponding to changes in the selection of the specific analogue samples, although  
104 this tendency is less marked in the conceptually analogous response surface technique (Bartlein  
105 et al., 1986). Regression-based techniques, including weighted averaging methods such as  
106 Weighted Average Partial Least-Squares (WAPLS: ter Braak and Juggins, 1993), do not  
107 produce step-changes in the reconstructions but suffer from the tendency to compress the  
108 reconstructions towards the central part of the sampled climate range. However, this tendency  
109 can be substantially reduced by accounting for the sampling frequency ( $fx$ ) and the climate  
110 tolerance of the pollen taxa present in the training data set (fxTWA-PLS: Liu et al., 2020).  
111 Machine-learning and Bayesian approaches have also been applied to derive climate  
112 reconstructions from pollen assemblages (Peyron et al., 1998; Salonen et al., 2019). However,  
113 comparison of fxTWA-PLS with the Bayesian model BUMPER (Holden et al., 2017), shows  
114 that fxTWA-PLS performs better in capturing the climate of the modern training data set from  
115 Europe (Liu et al., 2020).

116 Although fxTWA-PLS has clear advantages over other quantitative reconstructions techniques,  
117 there is still a slight tendency towards compression. We have therefore made a further  
118 modification to the approach as described in Liu et al. (2020). In the original version of  
119 fxTWA-PLS, the  $fx$  correction is applied as a weight with the form of  $1/fx^2$  in the regression  
120 (step 7 in Table 1 in Liu et al., 2020). Here (see Appendix A) we make a further modification  
121 of fxTWA-PLS by (a) applying the  $fx$  correction separately in both the taxon calculation and  
122 the regression (step 2 and 7 in Table 1 in Liu et al., 2020) as a weight with the form of  $1/fx$  and  
123 (b) applying P-splines smoothing (Eilers and Marx, 2021) in order to reduce the dependence  
124 of the  $fx$  estimation on bin width. The modified version further reduces the biases at the  
125 extremes of the sampled climate range.

126 There are no generally accepted rules as to the choice of variables for palaeoclimate  
127 reconstruction. No systematic comparison of these choices has been made. However, it is  
128 widely understood that plant taxon distributions reflect distinct, largely independent controls  
129 by summer temperature, winter temperature, and moisture availability (see e.g. Harrison et al.,  
130 2010). Therefore, in common with many other studies (Cheddadi et al., 1997; Jiang et al., 2010;  
131 Peyron et al., 1998; Wei et al., 2021; Zhang et al., 2007), we have chosen bioclimatic variables  
132 that reflect these independent controls, with mean temperature of the coldest month (MTCO)  
133 to represent winter temperature, mean temperature of the warmest month (MTWA) to represent  
134 summer temperature and  $\alpha$ , an estimate of the ratio of actual evapotranspiration to equilibrium  
135 evapotranspiration, to represent plant-available moisture. We choose not to use mean annual  
136 air temperature (MAAT) because it is a composite of summer and winter conditions; and we  
137 prefer to use an index of effective moisture availability (our estimate of  $\alpha$  being one such index)  
138 to mean annual precipitation (MAP), whose significance for plant function depends strongly  
139 on potential evaporation (a function of temperature and net radiation). Our calculation of  $\alpha$   
140 takes account of this dependence. Growing degree days above a baseline of 0 °C (GDD<sub>0</sub>) would  
141 be a possible alternative to MTWA as an expression of summer conditions but is most relevant  
142 as a predictor of “cold limits” of trees in cool climates, whereas MTWA better reflects the high-  
143 temperature stress on plants in Mediterranean-type climates.

144 We used the modified version of fxTWA-PLS to reconstruct these three climate variables. The  
145 individual and joint effects of MTCO, MTWA and  $\alpha$  were tested explicitly using canonical  
146 correspondence analysis (CCA). The modified version further reduces the biases at the  
147 extremes of the sampled climate range, while retaining the desirable properties of WA-PLS in  
148 terms of robustness to spatial autocorrelation (fxTWA-PLS: Liu et al., 2020).

149 The modern pollen training dataset was derived from the SPECIAL Modern Pollen Data Set  
150 (SMPDS: Harrison, 2019). The SMPDS consists of relative abundance records from 6458  
151 terrestrial sites from Europe, northern Africa, the Middle East and northern Eurasia (SI Fig.  
152 S1) assembled from multiple different published sources. The pollen records were  
153 taxonomically standardized, and filtered (as recommended by Chevalier et al., 2020) to remove  
154 obligate aquatics, insectivorous species, introduced species, and taxa that only occur in  
155 cultivation (see SI Table S1 for the list). Taxa (mainly herbaceous) with only sporadic  
156 occurrences were amalgamated to higher taxonomic levels (genus, sub-family or family) after  
157 ensuring consistency with their distribution in climate space. As a result of these

158 amalgamations, the SMPDS contains data on 247 pollen taxa. For our analysis, we use the 195  
159 taxa that occur at more than 10 sites.

160 Modern climate data at each of the sites in the training data set were obtained from Harrison  
161 (2019). This data set contains climate reconstructions of MTCO, growing degree days above a  
162 baseline of 0° C ( $GDD_0$ ) and a moisture index (MI), defined as the ratio of annual precipitation  
163 to annual potential evapotranspiration. The climate at each site was obtained using  
164 geographically weighted regression (GWR) of the CRU CL v2.0 gridded dataset of modern  
165 (1961-1990) surface climate at 10 arc minute resolution (New et al., 2002) in order to (a)  
166 correct for elevation differences between each pollen site and the corresponding grid cell and  
167 (b) make the resulting climate independent of the resolution of the underlying data set. The  
168 geographically weighted regression used a fixed bandwidth kernel of 1.06 ° (~140km) to  
169 optimize model diagnostics and reduce spatial clustering of residuals relative to other  
170 bandwidths. The climate of each pollen site was then estimated based on its longitude, latitude,  
171 and elevation. MTCO and  $GDD_0$  was taken directly from the GWR regression and MI was  
172 calculated for each pollen site using a modified code from SPLASH v1.0 (Davis et al., 2017)  
173 based on daily values of precipitation, temperature and sunshine hours again obtained using a  
174 mean-conserving interpolation of the monthly values of each. For this application, we used  
175 MTCO directly from the data set but calculated MTWA from MTCO and  $GDD_0$ , based on the  
176 relationship between MTCO, MTWA and  $GDD_0$  given in Appendix 2 of Wei et al. (2021). We  
177 derived  $\alpha$  from MI following Liu et al. (2020). The modern training data set provides records  
178 spanning a range of MTCO from – 42.4 °C to 14.8 °C, of MTWA from 4.2 °C to 33.5 °C, and  
179 of  $\alpha$  from 0.04 to 1.25 (Fig. 1, SI Fig. S1).

180 The fossil pollen data from the Iberian Peninsula were compiled by Shen et al. (2022) and the  
181 data set was obtained from Harrison et al. (2022). The taxonomy used by Shen et al. (2022) is  
182 consistent with that employed in the SMPDS. Shen et al. (2022) provides consistent age models  
183 for all the records based on the IntCal20 calibration curve (Reimer et al., 2020) and the BACON  
184 Bayesian age-modelling tool (Blaauw et al., 2021; Blaauw and Christeny, 2011) using the  
185 supervised modelling approach implemented in the `ageR` package (Villegas-Diaz et al, 2021).  
186 We excluded individual pollen samples with large uncertainties (standard error larger than 100  
187 years) on the ages attributed in the new age model. As a result, the climate reconstructions are  
188 based on a fossil data set of 7384 pollen samples from 117 records covering part or all of the  
189 last 12,000 years (Fig. 2), with 42 individual records provided by the original authors, 73

190 records obtained from the European Pollen Database (EPD, [www.europeanpollendatabase.net](http://www.europeanpollendatabase.net))  
191 and 2 records from PANGAEA ([www.pangaea.de/](http://www.pangaea.de/)). Details of the records are given in Table  
192 1. The average temporal resolution of these records is 101 years. We then excluded a few  
193 samples where the reconstructed values of  $\alpha$  exceed the natural limit of 0 and 1.26. Finally,  
194 7214 samples from 117 records are used for the analyses of the climate reconstructions.  
195 Summer insolation and winter insolation are also calculated using the PAST software based on  
196 the age and latitude of each sample (Hammer et al., 2001).

197 Variance inflation factor (VIF) scores are calculated for both the modern climates and the  
198 climates reconstructed from fossil pollen records, in order to avoid multicollinearity problems  
199 and thus guarantee the climate variables (MTCO, MTWA,  $\alpha$ ) used here represent independent  
200 features of the pollen records.

201 In addition to examining the reconstructions for individual sites, we constructed composite  
202 curves for the Iberian Peninsula as a whole. The composite curves provide a way of comparing  
203 the relationship between trends in the reconstructed climate changes and insolation changes.  
204 The curves were constructed after binning the site-based reconstructions using  $\pm 500$ -year bins.  
205 We used 1000 bootstrap resamplings of the reconstructed climate values in each  $\pm 500$ -year  
206 bin to avoid the influence of a single value or a single site on the mean climate value in this  
207 bin, and used the standard deviation of the 1000 values to represent the uncertainty of the mean  
208 climate value. We constructed linear regression plots to examine the longitudinal and  
209 elevational patterns in the reconstructed climate variables, and assessed the significance of  
210 differences in these trends through time compared to the most recent bin (0.5 ka  $\pm 500$  years)  
211 based on  $p$  values, with the customary threshold of 0.05. We then compared the climate trends  
212 with changes in summer and winter insolation.

### 213 3. Results

214 The modified version of fxTWA-PLS reproduces the modern climate reasonably well (Table  
215 2). The performance is best for MTCO ( $R^2$  0.75, RMSEP 4.70, slope 0.91) but is also good for  
216  $\alpha$  ( $R^2$  0.68, RMSEP 0.16, slope 0.78) and MTWA ( $R^2$  0.57, RMSEP 3.47, slope 0.71). The  
217 correlations between pollen records and each of the three bioclimate variables, as assessed by  
218 CCA, were strong for both modern climate data and fossil reconstructions (Table 3). The  
219 variance inflation factor (VIF) scores are all less than 6, so there are no multicollinearity  
220 problems (Table 3) (Allison, 1994), making it possible to reconstruct all three climate variables

221 independently based on pollen data. Furthermore, the taxa that contribute most strongly to  
222 reconstructing colder/warmer or wetter/drier climates show predictable patterns consistent with  
223 their known ecological preferences (SI Table S2).

224 Winters were generally colder than present during the early to mid-Holocene, as shown by the  
225 coherent patterns of reconstructed anomalies at individual sites (Fig. 3a, 3d). Here “present”  
226 means the most recent pollen bin ( $0.5 \text{ ka} \pm 500 \text{ years}$ ). The composite curve also shows a  
227 general increase in winter temperatures through time (Fig. 4a), consistent with the trend in  
228 winter insolation (Fig. 4d). The composite curve shows that it was ca  $4^\circ\text{C}$  cooler than today at  
229  $11.5 \text{ ka}$  but temperatures were only ca  $0.5^\circ\text{C}$  cooler than present after  $2.5 \text{ ka}$ . Winter  
230 temperatures today increase from north to south and are also affected by elevation; these  
231 patterns are still present in the Holocene reconstructions, but there is no spatial differentiation  
232 between western and eastern Iberia in the anomalies (Table 4, SI Fig. S2). The similarity of the  
233 changes compared to present geographically is consistent with the idea that the changes in  
234 winter temperature are driven by changes in winter insolation.

235 Summers were somewhat hotter than present in the west and cooler than present in the east  
236 during the early and mid-Holocene, as shown by the reconstructed anomalies at individual sites  
237 (Fig. 3b, 3e). This west-east difference could not arise if the changes in summer temperatures  
238 were a direct reflection of the insolation forcing (Fig. 4e). Indeed, the composite curve shows  
239 relatively little change in MTWA (Fig. 4b), confirming that there is no direct relationship to  
240 insolation forcing (Fig. 4e).

241 There is a strong west-east gradient in  $\alpha$  at the present day (Fig. 2), with wetter conditions in  
242 the west and drier conditions in the east. However, the reconstructed anomalies at individual  
243 sites (Fig. 3c, 3f) suggest that west was drier and the east was wetter than present in the mid-  
244 Holocene, resulting in a flatter west-east gradient. The west-east gradient is significantly  
245 different from present between  $9.5 \sim 3.5 \text{ ka}$  (Fig. 5, Table 4), implying stronger moisture  
246 advection into the continental interior during the mid-Holocene. The change in gradient is seen  
247 in both high and low elevation sites (SI Fig. S3). There is also significant change in  $\alpha$  with  
248 elevation between  $9.5 \sim 4.5 \text{ ka}$  (Table 4, SI Fig. S4).

249 Summer temperatures are strongly correlated with changes in  $\alpha$ , both in terms of spatial  
250 correlations in the modern data set at a European scale and in terms of spatial and temporal  
251 correlations in the fossil data set from Iberian Peninsula (Fig. 6). The patterns of reconstructed

252 anomalies in MTWA and  $\alpha$  at individual sites are also coherent (Fig. 3b, 3c, 3e, 3f), showing  
253 drier conditions and hotter summers in the west and wetter conditions with cooler summers in  
254 the east during the early to mid-Holocene. The west-east gradient in MTWA was significantly  
255 different from present between 9.5 and 3.5 ka except 8.5 ka (Table 4, SI Fig. S5), roughly the  
256 interval when the gradient in  $\alpha$  was also significantly different from present. Again, the change  
257 in the east-west gradient is registered at both high and low elevation sites (SI Fig. S6).  
258 However, there is no significant change in MTWA with elevation except 8.5 and 7.5 ka (Table  
259 4, SI Fig. S7).

#### 260 **4. Discussion**

261 The modified version of fxTWA-PLS (fxTWA-PLS2) (Table 2, Table A1) shows improved  
262 performance compared to the previous version (fxTWA-PLS1). Cross-validation  $R^2$  values are  
263 higher for MTCO and MTWA, but almost unchanged for  $\alpha$ . The maximum bias is decreased  
264 for all the three variables, especially for MTCO. The compression problem is also reduced for  
265 MTCO ( $b_1$  increases from 0.82 to 0.91) and MTWA ( $b_1$  increases from 0.69 to 0.71) while  
266 remaining roughly the same for  $\alpha$ . The overall performance statistics thus show substantial  
267 improvements for MTCO and MTWA, while they show little change for  $\alpha$ . However, Figure  
268 A1 shows that “non-physical” reconstructions beyond the natural limits of  $\alpha$  (0–1.26) are  
269 greatly reduced, especially at the lower limit. There are also fewer outliers in Figure A1 and  
270 A2 for all three variables. Thus overall, the modified version further reduces the reconstruction  
271 biases, especially at the extremes of the sampled climate range. This improvement probably  
272 occurs because of the separate application of 1/fx correction during both the calculation of  
273 optima and tolerances of taxa and during the regression step – instead of applying an overall  
274 weight of 1/fx<sup>2</sup> at the regression step, which can result in some extreme values (with low  
275 sampling frequency) being weighed too strongly and appearing as outliers.

276 The fxTWA-PLS2 reconstructions show that there was a gradual increase in MTCO over the  
277 Holocene, both for most of the individual sites represented in the data set (Fig. 3) and for Iberia  
278 as a whole (Fig. 4). Colder winters in southern Europe during the mid-Holocene (6 ka) are a  
279 feature of many earlier reconstructions (e.g. Cheddadi et al., 1997; Wu et al., 2007). A general  
280 warming trend over the Holocene is seen in gridded reconstructions of winter season  
281 (December, January, February) temperatures as reconstructed using the modern analogue  
282 approach by Mauri et al. (2015), although there is somewhat less millennial-scale variability  
283 in these reconstructions (Fig. 7). Nevertheless, their reconstructions show a cooling of 3°C in

284 the early Holocene, comparable in magnitude to the ca 4°C cooling at 11.5 ka reconstructed  
285 here. They show a gradual warming trend through the Holocene but the differences from  
286 present are very small (ca 0.5°C) after 2 ka, again consistent with our reconstructions of  
287 MTCO. Quantitative reconstructions of winter temperature for the 5 terrestrial sites from the  
288 Iberian Peninsula in the Kaufman et al. (2020) compilation all show a general trend of winter  
289 warming over the Holocene, but the magnitude of the change at some of the individual sites is  
290 much larger (ca 10°C) and there is no assessment of the uncertainty on these reconstructions.  
291 The composite curve of Kaufman et al. (2020) shows an increasing trend in MTCO through  
292 the Holocene although with large uncertainties (Fig. 7). In contrast to the consistency of the  
293 increasing trend in MTCO during the Holocene between our reconstructions and those of Mauri  
294 et al. (2015) and Kaufman et al. (2020), there is no discernible trend in MTCO during the  
295 Holocene reconstruction of Tarroso et al. (2016). Indeed, there is no significant change in their  
296 MTCO values after ca 9 ka, either for the Peninsula as a whole (Fig. 7) or for any of the four  
297 sub-regions they considered. Our reconstructed trend in winter temperature is consistent with  
298 the changes in insolation forcing at this latitude during the Holocene, and is also consistent  
299 with transient climate model simulations (Braconnot et al., 2019; Carré et al., 2021; Dallmeyer  
300 et al., 2020; Parker et al., 2021) of the winter temperature response to changing insolation  
301 forcing over the late Holocene in this region (Fig. 8, SI Fig. S8). Thus, we suggest that changes  
302 in winter temperatures are a direct consequence of insolation forcing.

303 We have shown that there is no overall trend in MTWA during the Holocene (Fig. 4).  
304 According to our reconstructions, summer temperatures fluctuated between ca 0.5°C above or  
305 below modern temperature. The lack of coherent trend in MTWA is consistent with the gridded  
306 reconstructions of summer (June, July, August) temperature in the Mauri et al. (2015) data set  
307 and also with the 5 terrestrial sites from Iberia included in the Kaufman et al. (2020) data set.  
308 However, the patterns shown in the three data sets are very different from one another. Mauri  
309 et al. (2015) suggest the early Holocene was colder than today, and although temperatures  
310 similar to today were reached at 9 ka, most of the Holocene was characterised by cooler  
311 summers. Kaufman et al. (2020), however, showed warmer than present conditions during the  
312 early Holocene although they also show cooler conditions during the later Holocene. The  
313 differences between the three data sets could reflect differences in the reconstruction methods,  
314 or differences in the number of records used and in the geographic sampling. However, given  
315 the fact that all three data sets show similar trends in winter temperature, the lack of coherency  
316 between the data sets for MTWA points to there not being a strong, regionally coherent signal

317 of summer temperature changes during the Holocene. Tarroso et al. (2016) also showed no  
318 significant changes in MTWA after ca 9 ka (Fig. 7).

319 The chironomid record from Laguna de la Roya covers the late glacial and terminates at 10.5  
320 ka (Muñoz Sobrino et al., 2013). The reconstructed July temperature during the early Holocene  
321 is ca 12~13 °C, which is considerably cooler than today at this site. However, the authors  
322 caution that these samples have poor analogues and the record should be interpreted with  
323 caution. Chironomid-based reconstructions of July temperature at Basa de la Mora (Tarrats et  
324 al., 2018), a high elevation site in the Pyrenees, indicate temperatures within  $\pm 0.5^\circ$  C of the  
325 modern during the early to mid-Holocene (10~6 ka), similar to our regional composite  
326 reconstructions. However, they show persistently conditions cooler than present by ca 1.5 °C  
327 between 4.5 and 2 ka, not seen in our reconstructions. Furthermore, direct comparison of our  
328 reconstructions of MTWA at Basa de la Mora (SI Fig. S9) to the chironomid-based  
329 reconstructions highlights that the two records show very different trajectories, since the  
330 pollen-based reconstruction of this site shows a consistent warming trend throughout the  
331 Holocene. Although Tarrats et al. (2018) argue that discrepancies between their temperature  
332 reconstructions and pollen-based reconstructions reflects the fact that the vegetation of Iberia,  
333 including the mountain areas, is largely driven by moisture changes and perhaps is not a good  
334 indicator of temperature, we have shown that there is sufficient information in the pollen  
335 records to reconstruct temperature and moisture independently (Table 3, Table S2). Thus, the  
336 cause of the differences between the pollen-based and chironomid-based reconstructions at  
337 Basa de la Mora is presumably related to methodology. In particular, the chironomid  
338 reconstructions use a training data set that does not include samples from the Pyrenees, or  
339 indeed the Mediterranean more generally, and may therefore not provide good analogues for  
340 Holocene changes at this site.

341 The lack of a clear trend in MTWA in our reconstructions (Fig. 4b) is not consistent with  
342 insolation forcing (Fig. 4e), which shows a declining trend during the Holocene nor is it  
343 consistent with simulated changes in MTWA in transient climate model simulations of the  
344 summer temperature response to changing insolation forcing over the Holocene in this region  
345 (Fig. 8). The change in moisture gradient during the mid-Holocene, however, suggests an  
346 alternative explanation whereby changes in summer temperature are a response to land-surface  
347 feedbacks associated with changes in moisture (Fig. 6). Specifically, the observed increased  
348 advection of moisture into eastern Iberia would have created wetter conditions there, which in

349 turn would permit increased evapotranspiration, implying less allocation of available net  
350 radiation to sensible heating, and resulting in cooler air temperatures. Our reconstructions show  
351 that the west-east moisture gradient in mid-Holocene (Fig. 5) was significantly flatter than the  
352 steep moisture gradient today (Fig. 2), implying a significant increase in moisture advection  
353 into the continental interior during this period. Mauri et al. (2015) also showed that summers  
354 were generally wetter than present in the east but drier than present in the west at early to mid-  
355 Holocene, supporting the idea of a flatter west-east gradient.

356 We have shown that stronger moisture advection is not a feature of transient climate model  
357 simulations of the Holocene, which may explain why these simulations do not show a strong  
358 modification of the insolation-driven changes in summer temperature (Fig. 8). Although the  
359 amplitude differs, all of the models show a general decline in summer temperature. The failure  
360 of the current generation of climate models to simulate the observed strengthening of moisture  
361 transport into Europe and Eurasia during the mid-Holocene has been noted for previous  
362 versions of these models (e.g. Bartlein et al., 2017; Mauri et al., 2014) and also shown in Fig.  
363 S8. Mauri et al. (2014), for example, showed that climate models participating in the last phase  
364 of the Coupled Model Intercomparison Project (CMIP5/PMIP3) were unable to reproduce  
365 reconstructed climate patterns over Europe at 6000 yr B.P. and indicated that this resulted from  
366 over-sensitivity to changes in insolation forcing and the failure to simulate increased moisture  
367 transport into the continent. Bartlein et al. (2017) showed that the CMIP5/PMIP3 models  
368 simulated warmer and drier conditions in mid-continental Eurasia at 6000 yr B.P., inconsistent  
369 with palaeo-environmental reconstructions from the region, as a result of the simulated  
370 reduction in the zonal temperature gradient which resulted in weaker westerly flow and reduced  
371 moisture fluxes into the mid-continent. They also pointed out the strong feedback between drier  
372 conditions and summer temperatures. The drying of the mid-continent is also a strong feature  
373 of the mid-Holocene simulations made with the current generation of CMIP6/PMIP4 models  
374 (Brierley et al., 2020). The persistence of these data-model mismatches highlights the need for  
375 better modelling of land-surface feedbacks on atmospheric circulation and moisture.

376 There are comparatively few pollen-based reconstructions of moisture changes during the  
377 Holocene from Iberia. Records from Padul show increased mean annual and winter  
378 precipitation during the early and mid-Holocene (Camuera et al., 2022; García-Alix et al.,  
379 2021). Reconstructions of mean annual and winter precipitation (Camuera et al., 2022) and the  
380 ratio of annual precipitation to annual potential evapotranspiration (Wei et al., 2021) also show

wetter conditions at this time at El Cañizar de Villarquemado. Both of these sites lie in the eastern part of the Iberian Peninsula, so these reconstructions are consistent with our interpretation of wetter conditions in this region during the interval between 9.5 and 3.5 ka. Ilvonen et al. (2022) provide pollen-based reconstructions of mean annual, summer and winter precipitation from 8 sites in Iberia, using WAPLS and a Bayesian modelling approach. Although they focus on the contrasting pattern of hydroclimate evolution between northern and southern Iberia, the three easternmost sites (San Rafael, Navarres, and Qintanar de la Sierra) show much wetter conditions during the early to mid-Holocene. With the exception of the record from Monte Areo, the records from further west are relatively complacent and indeed two sites (Zalamar, El Maillo) show decreased precipitation between 8 and 4 ka. Thus, these records are consistent with our interpretation that the west-east gradient of moisture was reduced between 9.5 and 3.5 ka (Figure 5).

Speleothem oxygen-isotope data from the Iberian Peninsula provide support for our pollen-based reconstructions of changes in the west-east gradient of moisture through the Holocene. The speleothem records show a progressive increase in temperature from the Younger Dryas onwards, although the trend is less marked in the west than the east (Baldini et al., 2019). This warming trend is consistent with our reconstructions of changes in MTCO through the Holocene. Speleothem records also show distinctly different patterns in moisture availability, with sites in western Iberia indicating wetter environments during early Holocene and a transition to drier conditions from ca 7.5 cal ka BP to the present (Stoll et al., 2013; Thatcher et al., 2020) while eastern sites record wetter conditions persisting from 9 to 4 cal ka (Walczak et al., 2015). This finding would support the weaker west to east moisture gradient shown by our results.

Pollen data are widely used for the quantitative reconstruction of past climates (see discussion in Bartlein et al., 2011), but reconstructions of moisture indices are also affected by changes in water-use efficiency caused by the impact of changing atmospheric CO<sub>2</sub> levels on plant physiology (Farquhar, 1997; Gerhart and Ward, 2010; Prentice et al., 2017; Prentice and Harrison, 2009). This has been shown to be important on glacial-interglacial timescales, when intervals of lower-than-present CO<sub>2</sub> result in vegetation appearing to reflect drier conditions than were experienced in reality (Prentice et al., 2011, 2017; Wei et al., 2021). We do not account for this CO<sub>2</sub> effect in our reconstructions of  $\alpha$  because the change in CO<sub>2</sub> over the Holocene was only 40 ppm. This change relative to modern levels has only a small impact on

413 the reconstructions (Prentice et al., 2022) and is sufficiently small to be within the  
414 reconstruction uncertainties. Furthermore, accounting for changes in CO<sub>2</sub> would not affect the  
415 reconstructed west-east gradient through time.

416 A more serious issue for our reconstructions may be the extent to which the vegetation cover  
417 of Iberia was substantially modified by human activities during the Holocene. Archaeological  
418 evidence shows that the introduction of agriculture during the Neolithic transition occurred ca  
419 7.6 ka in some southern and eastern areas of the Iberian Peninsula but spread slowly and  
420 farming first occurred only around 6 ka in the northwest (Drake et al., 2017; Fyfe et al., 2019;  
421 Zapata et al., 2004). Anthropogenic changes in land use have been detected at a number of  
422 sites, based on pollen evidence of increases in weeds or the presence of cereals (e.g. Abel-  
423 Schaad and López-Sáez, 2013; Cortés Sánchez et al., 2012; López-Merino et al., 2010; Mighall  
424 et al., 2006; Peña-Chocarro et al., 2005) or the presence of fungal spores associated with animal  
425 faeces which has been used to identify the presence of domesticated animals (e.g. López-Sáez  
426 and López-Merino, 2007; Revelles et al., 2018). The presence of cereals is the most reliable  
427 source of data on human activities, but most cereals only release pollen during threshing and  
428 thus are not found in abundance in pollen diagrams from natural (as opposed to archaeological)  
429 sites (Trondman et al., 2015). Indeed, it is only after ca 1 ka that the number of sites which  
430 record cereal pollen exceeds the number of sites at which cereals are not represented (Githumbi  
431 et al., 2022). Thus, while anthropogenic activities may have been important at the local scale  
432 and particularly in the later Holocene (e.g. Connor et al., 2019; Fyfe et al., 2019; Githumbi et  
433 al., 2022), most of the sites used for our reconstructions are not associated with archaeological  
434 evidence of agriculture or substantial landscape modification. Furthermore, the consistency of  
435 the reconstructed changes in climate across sites provides support for these being largely a  
436 reflection of regional climate changes rather than human activities.

437 We have used a modified version of fxTWA-PLS to reconstruct Holocene climates of the  
438 Iberian Peninsula because this modification reduced the compression bias in MTCO and  
439 MTWA, and specifically reduces the maximum bias in MTCO, MTWA and  $\alpha$ . Although this  
440 modified approach produces better overall reconstructions (Appendix A), its use does not  
441 change the reconstructed trends in these variables through time (SI Fig. S10). Thus, the finding  
442 that winter temperatures are a direct reflection of insolation forcing whereas summer  
443 temperatures are influenced by land-surface feedbacks and changes in atmospheric circulation  
444 is robust to the version of fxTWA-PLS used. However, while we use a much larger data set

445 than previous reconstructions, the distribution of pollen sites is uneven and the northern part  
446 of the Peninsula is better sampled than the southwest, which could lead to some uncertainties  
447 in the interpretation of changes in the west-east gradient of moisture. It would, therefore, be  
448 useful to specifically target the southwestern part of the Iberian Peninsula for new data  
449 collection. Alternatively, it would be useful to apply the approach used here to the whole of  
450 Eurasia, given that the failure of state-of-the-art climate models to advect moisture into the  
451 continental interior appears to be a feature of the whole region (Bartlein et al., 2017) and not  
452 the Peninsula alone.

453 **5. Conclusion**

454 We have developed an improved version of fxTWA-PLS which further reduces compression  
455 bias and provides robust climate reconstructions. We have used this technique with a large  
456 pollen data set representing 117 sites across the Iberian Peninsula to make quantitative  
457 reconstructions of summer and winter temperature and an index of plant-available moisture  
458 through the Holocene. We show that there was a gradual increase in winter temperature through  
459 the Holocene and that this trend broadly follows the changes in orbital forcing. Summer  
460 temperatures, however, do not follow the changes in orbital forcing but appear to be influenced  
461 by land-surface feedbacks associated with changes in moisture. We show that the west-east  
462 gradient in moisture was considerably less pronounced during the mid-Holocene, implying a  
463 significant increase in moisture advection into the continental interior resulting from changes  
464 in circulation. Our reconstructions of temperature changes are broadly consistent with previous  
465 reconstructions, but are more solidly based because of the increased site coverage. Our  
466 reconstructions of changes in the west-east gradient of moisture during the early part of the  
467 Holocene are also consistent with previous reconstructions, although this change is not  
468 simulated by state-of-the-art climate models, implying that there are still issues to resolve the  
469 associated land-surface feedbacks in these models. Our work provides an improved foundation  
470 for documenting and understanding the Holocene palaeoclimates of Iberia.

471

472 **Data and Code Availability**

473 All the data used are public access and cited here. The code used to generate the climate  
474 reconstructions is available at <https://github.com/ml4418/Iberia-paper.git>.

475 **Supplement.** The supplement related to this article is available online.

476 **Competing interests.** We declare that we have no conflict of interest.

477 **Author Contributions.** ML, ICP and SPH designed the study. ML, ICP and CJFtB designed  
478 the modifications to fxTWA-PLS. PG-S and GG-R provided pollen data and insights into the  
479 regional palaeoclimate histories. ML carried out the analyses. ML and SPH wrote the first  
480 draft of the paper and all authors contributed to the final draft.

481 **Acknowledgements.** ML acknowledges support from Imperial College through the Lee  
482 Family Scholarship. YS and SPH acknowledge support from the ERC-funded project GC 2.0  
483 (Global Change 2.0: Unlocking the past for a clearer future; grant number 694481). ICP  
484 acknowledges support from the ERC under the European Union Horizon 2020 research and  
485 innovation programme (grant agreement no: 787203 REALM). This work is a contribution to  
486 the project "Origen y Cuantification de los Cambios Paleoambientales en el Pirineo:  
487 Variabilidad climatic e impacto humano" (PYCACHU: PID2019-106050RB-I00)" funded by  
488 the Ministerio de Ciencia e Innovación.

489 **Financial support.** This research has been supported by Lee Family Scholarship fund, and  
490 the European Research Council (grant no. GC2.0, 694481, and grant no. REALM, 787203).

491 **References**

492 Abel-Schaad, D. and López-Sáez, J. A.: Vegetation changes in relation to fire history and  
 493 human activities at the Peña Negra mire (Bejar Range, Iberian Central Mountain System,  
 494 Spain) during the past 4,000 years, *Veg. Hist. Archaeobot.*, 22, 199–214,  
 495 doi:10.1007/s00334-012-0368-9, 2013.

496 Allison, P. D.: *Multiple Regression: A Primer*, Pine Forge Press., 1994.

497 Andrade, C., Contente, J. and Santos, J. A.: Climate change projections of aridity conditions  
 498 in the Iberian Peninsula, *Water*, 13(15), doi:10.3390/w13152035, 2021a.

499 Andrade, C., Contente, J. and Santos, J. A.: Climate change projections of dry and wet events  
 500 in Iberia based on the WASP-Index, *Climate*, 9(6), doi:10.3390/cli9060094, 2021b.

501 Aranbarri, J., Gonzalez Samperiz, P., Valero-Garcés, B., Moreno, A., Gil-Romera, G.,  
 502 Sevilla-Callejo, M., García-Prieto, E., Di Rita, F., Mata, M. del Pi., Morellón, M., Magri, D.,  
 503 Rodríguez-Lázaro, J. and Carrión, J.: Rapid climatic changes and resilient vegetation during  
 504 the Lateglacial and Holocene in a continental region of south-western Europe, *Glob. Planet.  
 505 Change*, 114, 50–65, doi:10.1016/j.gloplacha.2014.01.003, 2014.

506 Aranbarri, J., González-Sampériz, P., Iriarte, E., Moreno, A., Rojo-Guerra, M., Peña-  
 507 Chocarro, L., Valero-Garcés, B., Leunda, M., García-Prieto, E., Sevilla-Callejo, M., Gil-  
 508 Romera, G., Magri, D. and Rodríguez-Lázaro, J.: Human–landscape interactions in the  
 509 Conquezuela–Ambrona Valley (Soria, continental Iberia): From the early Neolithic land use  
 510 to the origin of the current oak woodland, *Palaeogeogr. Palaeoclimatol. Palaeoecol.*, 436, 41–  
 511 57, doi:<https://doi.org/10.1016/j.palaeo.2015.06.030>, 2015.

512 Baldini, L. M., Baldini, J. U. L., McDermott, F., Arias, P., Cueto, M., Fairchild, I. J.,  
 513 Hoffmann, D. L., Mattey, D. P., Müller, W., Nita, D. C., Ontañón, R., Garcíá-Moncó, C. and  
 514 Richards, D. A.: North Iberian temperature and rainfall seasonality over the Younger Dryas  
 515 and Holocene, *Quat. Sci. Rev.*, 226, 105998,  
 516 doi:<https://doi.org/10.1016/j.quascirev.2019.105998>, 2019.

517 Bartlein, P. J., Prentice, I. C. and Webb, T.: Climatic response surfaces from pollen data for  
 518 some Eastern North American taxa, *J. Biogeogr.*, 13(1), 35, doi:10.2307/2844848, 1986.

519 Bartlein, P. J., Harrison, S. P., Brewer, S., Connor, S., Davis, B. A. S., Gajewski, K., Guiot,  
 520 J., Harrison-Prentice, T. I., Henderson, A., Peyron, O., Prentice, I. C., Scholze, M., Seppä, H.,  
 521 Shuman, B., Sugita, S., Thompson, R. S., Viau, A. E., Williams, J. and Wu, H.: Pollen-based  
 522 continental climate reconstructions at 6 and 21 ka: A global synthesis, *Clim. Dyn.*, 37(3),  
 523 775–802, doi:10.1007/s00382-010-0904-1, 2011.

524 Bartlein, P. J., Harrison, S. P. and Izumi, K.: Underlying causes of Eurasian midcontinental  
 525 aridity in simulations of mid-Holocene climate, *Geophys. Res. Lett.*, 44(17), 9020–9028,  
 526 doi:10.1002/2017GL074476, 2017.

527 Blaauw, M. and Christeny, J. A.: Flexible paleoclimate age-depth models using an  
 528 autoregressive gamma process, *Bayesian Anal.*, 6(3), 457–474, doi:10.1214/11-BA618, 2011.

529 Blaauw, M., Christen, J. A., Lopez, M. A. A. V., V., J. E. O. M. G., Belding, T., Theiler, J.,  
 530 Gough, B. and Karney, C.: *rbacon*: Age-depth modelling using Bayesian statistics, [online]  
 531 Available from: <https://cran.r-project.org/package=rbacon>, 2021.

532 ter Braak, C. J. F. and Juggins, S.: Weighted averaging partial least squares regression (WA-  
 533 PLS): An improved method for reconstructing environmental variables from species  
 534 assemblages, *Hydrobiologia*, 269(1), 485–502, doi:10.1007/BF00028046, 1993.

535 Braconnot, P., Crétat, J., Marti, O., Balkanski, Y., Caubel, A., Cozic, A., Foujols, M.-A. and  
 536 Sanogo, S.: Impact of multiscale variability on last 6,000 years Indian and West African  
 537 monsoon rain, *Geophys. Res. Lett.*, 46(23), 14021–14029,  
 538 doi:<https://doi.org/10.1029/2019GL084797>, 2019.

539 Brierley, C. M., Zhao, A., Harrison, S. P., Braconnot, P., Williams, C. J. R., Thornalley, D. J.  
 540 R., Shi, X., Peterschmitt, J.-Y., Ohgaito, R., Kaufman, D. S., Kageyama, M., Hargreaves, J.  
 541 C., Erb, M. P., Emile-Geay, J., D'Agostino, R., Chandan, D., Carré, M., Bartlein, P., Zheng,  
 542 W., Zhang, Z., Zhang, Q., Yang, H., Volodin, E. M., Tomas, R. A., Routson, C., Peltier, W.  
 543 R., Otto-Bliesner, B., Morozova, P. A., McKay, N. P., Lohmann, G., Legrande, A. N., Guo,  
 544 C., Cao, J., Brady, E., Annan, J. D. and Abe-Ouchi, A.: Large-scale features and evaluation  
 545 of the PMIP4-CMIP6 midHolocene simulations, *Clim. Past*, 16, 1847–1872, doi:10.5194/cp-  
 546 16-1847-2020, 2020.

547 Camuera, J., Ramos-Román, M. J., Jiménez-Moreno, G., García-Alix, A., Ilvonen, L., Ruha,  
 548 L., Gil-Romera, G., González-Sampériz, P. and Seppä, H.: Past 200 kyr hydroclimate  
 549 variability in the western Mediterranean and its connection to the African Humid Periods,  
 550 *Sci. Rep.*, 12(1), 9050, doi:10.1038/s41598-022-12047-1, 2022.

551 Carré, M., Braconnot, P., Elliot, M., d'Agostino, R., Schurer, A., Shi, X., Marti, O.,  
 552 Lohmann, G., Jungclaus, J., Cheddadi, R., Abdelkader di Carlo, I., Cardich, J., Ochoa, D.,  
 553 Salas Gismondi, R., Pérez, A., Romero, P. E., Turcq, B., Corrège, T. and Harrison, S. P.:  
 554 High-resolution marine data and transient simulations support orbital forcing of ENSO  
 555 amplitude since the mid-Holocene, *Quat. Sci. Rev.*, 268, 107125,  
 556 doi:<https://doi.org/10.1016/j.quascirev.2021.107125>, 2021.

557 Carrión, J. S., Fernández, S., González-Sampériz, P., Gil-Romera, G., Badal, E., Carrión-  
 558 Marco, Y., López-Merino, L., López-Sáez, J. A., Fierro, E. and Burjachs, F.: Expected trends  
 559 and surprises in the Lateglacial and Holocene vegetation history of the Iberian Peninsula and  
 560 Balearic Islands, *Rev. Palaeobot. Palynol.*, 162(3), 458–475,  
 561 doi:<https://doi.org/10.1016/j.revpalbo.2009.12.007>, 2010.

562 Carrión, Y., Kaal, J., López-Sáez, J. A., López-Merino, L. and Martínez Cortizas, A.:  
 563 Holocene vegetation changes in NW Iberia revealed by anthracological and palynological  
 564 records from a colluvial soil, *The Holocene*, 20(1), 53–66, doi:10.1177/0959683609348849,  
 565 2009.

566 Carvalho, D., Pereira, S. and Rocha, A.: Future surface temperature changes for the Iberian  
 567 Peninsula according to EURO-CORDEX climate projections, *Clim. Dyn.*, 56, 1–16,  
 568 doi:10.1007/s00382-020-05472-3, 2021.

569 Cheddadi, R., Yu, G., Guiot, J., Harrison, S.P., and Prentice, I.C.: The climate of Europe  
 570 6000 years ago, *Clim. Dyn.*, 13, 1, doi:10.1007/s003820050148, 1997.

571 Chevalier, M., Davis, B. A. S., Heiri, O., Seppä, H., Chase, B. M., Gajewski, K., Lacourse,  
 572 T., Telford, R. J., Finsinger, W., Guiot, J., Kühl, N., Maezumi, S. Y., Tipton, J. R., Carter, V.  
 573 A., Brussel, T., Phelps, L. N., Dawson, A., Zanon, M., Vallé, F., Nolan, C., Mauri, A., de  
 574 Vernal, A., Izumi, K., Holmström, L., Marsicek, J., Goring, S., Sommer, P. S., Chaput, M.  
 575 and Kupriyanov, D.: Pollen-based climate reconstruction techniques for late Quaternary  
 576 studies, *Earth-Science Rev.*, 210, 103384,  
 577 doi:<https://doi.org/10.1016/j.earscirev.2020.103384>, 2020.

578 Connor, S., Vannière, B., Colombaroli, D., Anderson, R., Carrión, J., Ejarque, A., Gil-  
 579 Romera, G., Gonzalez Samperiz, P., Höfer, D., Morales-Molino, C., Revelles, J., Schneider,  
 580 H., Knaap, W., Leeuwen, J., and Woodbridge, J.: Humans take control of fire-driven  
 581 diversity changes in Mediterranean Iberia's vegetation during the mid–late Holocene, *The  
 582 Holocene*, 29, 095968361982665, doi:10.1177/0959683619826652, 2019.

583 Cortés Sánchez, M., Jiménez Espejo, F. J., Simón Vallejo, M. D., Gibaja Bao, J. F., Carvalho,  
 584 A. F., Martínez-Ruiz, F., Gamiz, M. R., Flores, J.-A., Paytan, A., López Sáez, J. A., Peña-  
 585 Chocarro, L., Carrión, J. S., Morales Muñiz, A., Roselló Izquierdo, E., Riquelme Cantal, J.  
 586 A., Dean, R. M., Salgueiro, E., Martínez Sánchez, R. M., De la Rubia de Gracia, J. J., Lozano  
 587 Francisco, M. C., Vera Peláez, J. L., Rodríguez, L. L. and Bicho, N. F.: The Mesolithic–  
 588 Neolithic transition in southern Iberia, *Quat. Res.*, 77(2), 221–234,  
 589 doi:<https://doi.org/10.1016/j.yqres.2011.12.003>, 2012.

590 Dallmeyer, A., Claussen, M., Lorenz, S. J. and Shanahan, T.: The end of the African humid  
 591 period as seen by a transient comprehensive Earth system model simulation of the last 8000  
 592 years, *Clim. Past*, 16, 117–140, doi:10.5194/cp-2019-86, 2020.

593 Davis, B. A. S., Brewer, S., Stevenson, A. C. and Guiot, J.: The temperature of Europe during  
 594 the Holocene reconstructed from pollen data, *Quat. Sci. Rev.*, 22(15), 1701–1716,  
 595 doi:[https://doi.org/10.1016/S0277-3791\(03\)00173-2](https://doi.org/10.1016/S0277-3791(03)00173-2), 2003.

596 Davis, T. W., Prentice, I. C., Stocker, B. D., Thomas, R. T., Whitley, R. J., Wang, H., Evans,  
 597 B. J., Gallego-Sala, A. V., Sykes, M. T. and Cramer, W.: Simple process-led algorithms for  
 598 simulating habitats (SPLASH v.1.0): Robust indices of radiation, evapotranspiration and  
 599 plant-available moisture, *Geosci. Model Dev.*, 10(2), 689–708, doi:10.5194/gmd-10-689-  
 600 2017, 2017.

601 Drake, B. L., Blanco-González, A. and Lillios, K. T.: Regional demographic dynamics in the  
 602 Neolithic Transition in Iberia: Results from summed calibrated date analysis, *J. Archaeol.  
 603 Method Theory*, 24(3), 796–812, doi:10.1007/s10816-016-9286-y, 2017.

604 Eilers, P. H. and Marx, B. D.: Practical smoothing: The Joys of P-splines, edited by P. H.  
 605 Eilers and B. D. Marx, Cambridge University Press., 2021.

606 Farquhar, G. D.: Carbon dioxide and vegetation, *Science*, 278(5342), 1411,  
 607 doi:10.1126/science.278.5342.1411, 1997.

608 Fyfe, R. M., Woodbridge, J., Palmisano, A., Bevan, A., Shennan, S., Burjachs, F., Legarra  
 609 Herrero, B., García Puchol, O., Carrión, J. S., Revelles, J. and Roberts, C. N.: Prehistoric  
 610 palaeodemographics and regional land cover change in eastern Iberia, *Holocene*, 29(5), 799–  
 611 815, doi:10.1177/0959683619826643, 2019.

612 García-Alix, A., Camuera, J., Ramos-Román, M. J., Toney, J. L., Sachse, D., Schefuß, E.,  
 613 Jiménez-Moreno, G., Jiménez-Espejo, F. J., López-Avilés, A., Anderson, R. S. and Yanes,  
 614 Y.: Paleohydrological dynamics in the Western Mediterranean during the last glacial cycle,  
 615 *Glob. Planet. Change*, 202, 103527, doi:<https://doi.org/10.1016/j.gloplacha.2021.103527>,  
 616 2021.

617 Gerhart, L. M. and Ward, J. K.: Plant responses to low [CO<sub>2</sub>] of the past, *New Phytol.*,  
 618 188(3), 674–695, doi:<https://doi.org/10.1111/j.1469-8137.2010.03441.x>, 2010.

619 Githumbi, E., Fyfe, R., Gaillard, M.-J., Trondman, A.-K., Mazier, F., Nielsen, A.-B., Poska,  
 620 A., Sugita, S., Woodbridge, J., Azuara, J., Feurdean, A., Grindean, R., Lebreton, V.,  
 621 Marquer, L., Nebout-Combourieu, N., Stančikaitė, M., Tančūau, I., Tonkov, S.,  
 622 Shumilovskikh, L. and data contributors, L.: European pollen-based REVEALS land-cover  
 623 reconstructions for the Holocene: methodology, mapping and potentials, *Earth Syst. Sci.  
 624 Data*, 14(4), 1581–1619, doi:10.5194/essd-14-1581-2022, 2022.

625 González-Sampériz, P., Aranbarri, J., Pérez-Sanz, A., Gil-Romera, G., Moreno, A., Leunda,  
 626 M., Sevilla-Callejo, M., Corella, J. P., Morellón, M., Oliva, B. and Valero-Garcés, B.:  
 627 Environmental and climate change in the southern Central Pyrenees since the Last Glacial  
 628 Maximum: A view from the lake records, *Catena*, 149, 668–688,  
 629 doi:<https://doi.org/10.1016/j.catena.2016.07.041>, 2017.

630 Granados, I. and Toro, M.: Recent warming in a high mountain lake (Laguna Cimera, Central  
 631 Spain) inferred by means of fossil chironomids, *J. Limnol.*, 59 (suppl., 109–119,  
 632 doi:10.4081/limnol.2000.s1.109, 2000.

633 Hammer, O., Harper, D. and Ryan, P.: PAST: Paleontological statistics software package for  
 634 education and data analysis, *Palaeontol. Electron.*, 4, 1–9, 2001.

635 Harrison, S.P., Shen, Y. and Sweeney, L.: Pollen data and charcoal data of the Iberian  
 636 Peninsula (version 3), [online] Available from: <https://doi.org/10.17864/1947.000369>, 2022.

637 Harrison, S. P.: Modern pollen data for climate reconstructions, version 1 (SMPDS), ,  
 638 doi:<http://dx.doi.org/10.17864/1947.194>, 2019.

639 Harrison, S. P., Prentice, I. C., Barboni, D., Kohfeld, K. E., Ni, J. and Sutra, J.-P.:

640 Ecophysiological and bioclimatic foundations for a global plant functional classification, J.  
 641 *Veg. Sci.*, 21(2), 300–317, doi:10.1111/j.1654-1103.2009.01144.x, 2010.

642 Holden, P. B., Birks, H. J. B., Brooks, S. J., Bush, M. B., Hwang, G. M., Matthews-Bird, F.,  
 643 Valencia, B. G. and van Woesik, R.: BUMPER v1.0: a Bayesian user-friendly model for  
 644 palaeo-environmental reconstruction, *Geosci. Model Dev.*, 10(1), 483–498,  
 645 doi:10.5194/gmd-10-483-2017, 2017.

646 Ilvonen, L., López-Sáez, J. A., Holmström, L., Alba-Sánchez, F., Pérez-Díaz, S., Carrión, J.  
 647 S., Ramos-Román, M. J., Camuera, J., Jiménez-Moreno, G., Ruha, L. and Seppä, H.: Spatial  
 648 and temporal patterns of Holocene precipitation change in the Iberian Peninsula, *Boreas*, 51,  
 649 776–792, doi:<https://doi.org/10.1111/bor.12586>, 2022.

650 Jiang, W., Guiot, J., Chu, G., Wu, H., Yuan, B., Hatté, C. and Guo, Z.: An improved  
 651 methodology of the modern analogues technique for palaeoclimate reconstruction in arid and  
 652 semi-arid regions, *Boreas*, 39(1), 145–153, doi:<https://doi.org/10.1111/j.1502-3885.2009.00115.x>, 2010.

654 Kaufman, D., McKay, N., Routson, C., Erb, M., Davis, B., Heiri, O., Jaccard, S., Tierney, J.,  
 655 Dätwyler, C., Axford, Y., Brussel, T., Cartapanis, O., Chase, B., Dawson, A., de Vernal, A.,  
 656 Engels, S., Jonkers, L., Marsicek, J., Moffa-Sánchez, P., Morrill, C., Orsi, A., Rehfeld, K.,  
 657 Saunders, K., Sommer, P. S., Thomas, E., Tonello, M., Tóth, M., Vachula, R., Andreev, A.,  
 658 Bertrand, S., Biskaborn, B., Bringué, M., Brooks, S., Caniupán, M., Chevalier, M., Cwynar,  
 659 L., Emile-Geay, J., Fegyveresi, J., Feurdean, A., Finsinger, W., Fortin, M.-C., Foster, L., Fox,  
 660 M., Gajewski, K., Grosjean, M., Hausmann, S., Heinrichs, M., Holmes, N., Ilyashuk, B.,  
 661 Ilyashuk, E., Juggins, S., Khider, D., Koinig, K., Langdon, P., Larocque-Tobler, I., Li, J.,  
 662 Lotter, A., Luoto, T., Mackay, A., Magyari, E., Malevich, S., Mark, B., Massaferro, J.,  
 663 Montade, V., Nazarova, L., Novenko, E., Paril, P., Pearson, E., Peros, M., Pienitz, R.,  
 664 Płociennik, M., Porinchu, D., Potito, A., Rees, A., Reinemann, S., Roberts, S., Rolland, N.,  
 665 Salonen, S., Self, A., Seppä, H., Shala, S., St-Jacques, J.-M., Stenni, B., Syrykh, L., Tarrats,  
 666 P., Taylor, K., van den Bos, V., Velle, G., Wahl, E., Walker, I., Wilmshurst, J., Zhang, E. and  
 667 Zhilich, S.: A global database of Holocene paleotemperature records, *Sci. Data*, 7(1), 115,  
 668 doi:10.1038/s41597-020-0445-3, 2020.

669 Liu, M., Prentice, I. C., ter Braak, C. J. F. and Harrison, S. P.: An improved statistical  
 670 approach for reconstructing past climates from biotic assemblages, *Proc. R. Soc. A Math.*,  
 671 476(2243), doi:<https://doi.org/10.1098/rspa.2020.0346>, 2020.

672 López-Merino, L., Cortizas, A. M. and López-Sáez, J. A.: Early agriculture and  
 673 palaeoenvironmental history in the North of the Iberian Peninsula: a multi-proxy analysis of  
 674 the Monte Areo mire (Asturias, Spain), *J. Archaeol. Sci.*, 37(8), 1978–1988,  
 675 doi:<https://doi.org/10.1016/j.jas.2010.03.003>, 2010.

676 López-Sáez, J. A. and López-Merino, L.: Coprophilous fungi as a source of information of  
 677 anthropic activities during the Prehistory in the Amblés Valley (Ávila, Spain): The  
 678 archaeopaleontological record, *Rev. Española Micropaleontol.*, 38, 49–75, 2007.

679 Martínez-Cortizas, A., Costa-Casais, M. and López-Sáez, J. A.: Environmental change in

680 NW Iberia between 7000 and 500 cal BC, *Quat. Int.*, 200(1), 77–89,  
681 doi:<https://doi.org/10.1016/j.quaint.2008.07.012>, 2009.

682 Mauri, A., Davis, B. A. S., Collins, P. M. and Kaplan, J. O.: The influence of atmospheric  
683 circulation on the mid-Holocene climate of Europe: a data–model comparison, *Clim. Past*,  
684 10(5), 1925–1938, doi:10.5194/cp-10-1925-2014, 2014.

685 Mauri, A., Davis, B. A. S., Collins, P. M. and Kaplan, J. O.: The climate of Europe during the  
686 Holocene: A gridded pollen-based reconstruction and its multi-proxy evaluation, *Quat. Sci.*  
687 *Rev.*, 112, 109–127, doi:10.1016/j.quascirev.2015.01.013, 2015.

688 Mighall, T. M., Martínez Cortizas, A., Biester, H. and Turner, S. E.: Proxy climate and  
689 vegetation changes during the last five millennia in NW Iberia: Pollen and non-pollen  
690 palynomorph data from two ombrotrophic peat bogs in the North Western Iberian Peninsula,  
691 *Rev. Palaeobot. Palynol.*, 141(1–2), 203–223, doi:10.1016/j.revpalbo.2006.03.013, 2006.

692 Millet, L., Rius, D., Galop, D., Heiri, O. and Brooks, S. J.: Chironomid-based reconstruction  
693 of Lateglacial summer temperatures from the Ech palaeolake record (French western  
694 Pyrenees), *Palaeogeogr. Palaeoclimatol. Palaeoecol.*, 315–316, 86–99,  
695 doi:<https://doi.org/10.1016/j.palaeo.2011.11.014>, 2012.

696 Morellón, M., Aranbarri, J., Moreno, A., González-Sampériz, P. and Valero-Garcés, B. L.:  
697 Early Holocene humidity patterns in the Iberian Peninsula reconstructed from lake, pollen  
698 and speleothem records, *Quat. Sci. Rev.*, 181, 1–18,  
699 doi:<https://doi.org/10.1016/j.quascirev.2017.11.016>, 2018.

700 Muñoz Sobrino, C., Heiri, O., Hazekamp, M., van der Velden, D., Kirilova, E. P., García-  
701 Moreiras, I. and Lotter, A. F.: New data on the Lateglacial period of SW Europe: a high  
702 resolution multiproxy record from Laguna de la Roya (NW Iberia), *Quat. Sci. Rev.*, 80, 58–  
703 77, doi:<https://doi.org/10.1016/j.quascirev.2013.08.016>, 2013.

704 New, M., Lister, D. and Hulme, M.: A high-resolution data set of surface climate over global  
705 land areas, *Clim. Res.*, 21(1), 1–25, 2002.

706 Overpeck, J. T., Webb, T. and Prentice, I. C.: Quantitative interpretation of fossil pollen  
707 spectra: Dissimilarity coefficients and the method of modern analogs, *Quat. Res.*, 23(1), 87–  
708 108, doi:10.1016/0033-5894(85)90074-2, 1985.

709 Parker, S. E., Harrison, S. P. and Braconnot, P.: Speleothem records of monsoon interannual-  
710 interdecadal variability through the Holocene, *Environ. Res. Commun.*, 3(12), 121002,  
711 doi:10.1088/2515-7620/ac3eaa, 2021.

712 Peña-Chocarro, L., Peña, L. Z., Gazolaz, J. G., Morales, M. G., Sesma, J. S. and Straus, L.  
713 G.: The spread of agriculture in northern Iberia: new archaeobotanical data from El Mirón  
714 cave (Cantabria) and the open-air site of Los Cascajos (Navarra), *Veg. Hist. Archaeobot.*,  
715 14(4), 268–278, doi:10.1007/s00334-005-0078-7, 2005.

716 Peyron, O., Guiot, J., Cheddadi, R., Tarasov, P., Reille, M., de Beaulieu, J.-L., Bottema, S.  
 717 and Andrieu, V.: Climatic reconstruction in Europe for 18,000 yr B.P. from pollen data, *Quat.*  
 718 *Res.*, 49(2), 183–196, doi:<https://doi.org/10.1006/qres.1997.1961>, 1998.

719 Prentice, I. C. and Harrison, S. P.: Ecosystem effects of CO<sub>2</sub> concentration: evidence from  
 720 past climates, *Clim. Past*, 5(3), 297–307, doi:10.5194/cp-5-297-2009, 2009.

721 Prentice, I. C., Meng, T., Wang, H., Harrison, S. P., Ni, J. and Wang, G.: Evidence of a  
 722 universal scaling relationship for leaf CO<sub>2</sub> drawdown along an aridity gradient, *New Phytol.*,  
 723 190(1), 169–180, doi:<https://doi.org/10.1111/j.1469-8137.2010.03579.x>, 2011.

724 Prentice, I. C., Cleator, S. F., Huang, Y. H., Harrison, S. P. and Roulstone, I.: Reconstructing  
 725 ice-age palaeoclimates: Quantifying low-CO<sub>2</sub> effects on plants, *Glob. Planet. Change*, 149,  
 726 166–176, doi:<https://doi.org/10.1016/j.gloplacha.2016.12.012>, 2017.

727 Prentice, I. C., Villegas-Diaz, R. and Harrison, S. P.: Accounting for atmospheric carbon  
 728 dioxide variations in pollen-based reconstruction of past hydroclimates, *Glob. Planet.*  
 729 *Change*, 211, 103790, 2022.

730 Ramos-Román, M. J., Jiménez-Moreno, G., Camuera, J., García-Alix, A., Anderson, R.,  
 731 Jiménez-Espejo, F., Sachse, D., Jaime, T., Carrión, J., Webster, C. and Yanes, Y.: Millennial-  
 732 scale cyclical environment and climate variability during the Holocene in the western  
 733 Mediterranean region deduced from a new multi-proxy analysis from the Padul record (Sierra  
 734 Nevada, Spain), *Glob. Planet. Change*, 168, doi:10.1016/j.gloplacha.2018.06.003, 2018.

735 Reimer, P. J., Austin, W. E. N., Bard, E., Bayliss, A., Blackwell, P. G., Bronk Ramsey, C.,  
 736 Butzin, M., Cheng, H., Edwards, R. L., Friedrich, M., Grootes, P. M., Guilderson, T. P.,  
 737 Hajdas, I., Heaton, T. J., Hogg, A. G., Hughen, K. A., Kromer, B., Manning, S. W.,  
 738 Muscheler, R., Palmer, J. G., Pearson, C., Van Der Plicht, J., Reimer, R. W., Richards, D. A.,  
 739 Scott, E. M., Southon, J. R., Turney, C. S. M., Wacker, L., Adolphi, F., Büntgen, U., Capano,  
 740 M., Fahrni, S. M., Fogtmann-Schulz, A., Friedrich, R., Köhler, P., Kudsk, S., Miyake, F.,  
 741 Olsen, J., Reinig, F., Sakamoto, M., Sookdeo, A. and Talamo, S.: The IntCal20 Northern  
 742 Hemisphere radiocarbon age calibration curve (0–55 cal kBP), *Radiocarbon*, 62(4), 725–757,  
 743 doi:10.1017/RDC.2020.41, 2020.

744 Revelles, J., Burjachs, F., Palomo, A., Piqué, R., Iriarte, E., Pérez-Obiol, R. and Terradas, X.:  
 745 Human-environment interaction during the Mesolithic-Neolithic transition in the NE Iberian  
 746 Peninsula. Vegetation history, climate change and human impact during the Early-Middle  
 747 Holocene in the Eastern Pre-Pyrenees, *Quat. Sci. Rev.*, 184, 183–200,  
 748 doi:<https://doi.org/10.1016/j.quascirev.2017.08.025>, 2018.

749 Salonen, J. S., Ilvonen, L., Seppä, H., Holmström, L., Telford, R. J., Gaidamavičius, A.,  
 750 Stančikaitė, M. and Subetto, D.: Comparing different calibration methods (WA/WA-PLS  
 751 regression and Bayesian modelling) and different-sized calibration sets in pollen-based  
 752 quantitative climate reconstruction, *The Holocene*, 22(4), 413–424,  
 753 doi:10.1177/0959683611425548, 2011.

754 Salonen, J. S., Korpela, M., Williams, J. W. and Luoto, M.: Machine-learning based  
 755 reconstructions of primary and secondary climate variables from North American and  
 756 European fossil pollen data, *Sci. Rep.*, 9(1), 15805, doi:10.1038/s41598-019-52293-4, 2019.

757 Schröder, T., López-Sáez, J. A., van't Hoff, J. and Reicherter, K.: Unravelling the Holocene  
 758 environmental history of south-western Iberia through a palynological study of Lake Medina  
 759 sediments, *The Holocene*, 30(1), 13–22, doi:10.1177/0959683619865590, 2019.

760 Shen, Y., Sweeney, L., Liu, M., Lopez Saez, J. A., Pérez-Díaz, S., Luelmo-Lautenschlaeger,  
 761 R., Gil-Romera, G., Hoefer, D., Jiménez-Moreno, G., Schneider, H., Prentice, I. C. and  
 762 Harrison, S. P.: Reconstructing burnt area during the Holocene: an Iberian case study, *Clim.*  
 763 *Past*, 18, 1189–1201, doi:10.5194/cp-18-1189-2022, 2022.

764 Stoll, H. M., Moreno, A., Mendez-Vicente, A., Gonzalez-Lemos, S., Jimenez-Sanchez, M.,  
 765 Dominguez-Cuesta, M. J., Edwards, R. L., Cheng, H. and Wang, X.: Paleoclimate and  
 766 growth rates of speleothems in the northwestern Iberian Peninsula over the last two glacial  
 767 cycles, *Quat. Res.*, 80, 284–290, doi:10.1016/j.yqres.2013.05.002, 2013.

768 Tarrats, P., Heiri, O., Valero-Garcés, B., Cañedo-Argüelles, M., Prat, N., Rieradevall, M. and  
 769 González-Sampériz, P.: Chironomid-inferred Holocene temperature reconstruction in Basa de  
 770 la Mora Lake (Central Pyrenees), *The Holocene*, 28(11), 1685–1696,  
 771 doi:10.1177/0959683618788662, 2018.

772 Tarroso, P., Carrión, J., Dorado-Valiño, M., Queiroz, P., Santos, L., Valdeolmillos-  
 773 Rodríguez, A., Célio Alves, P., Brito, J. C. and Cheddadi, R.: Spatial climate dynamics in the  
 774 Iberian Peninsula since 15 000 yr BP, *Clim. Past*, 12(5), 1137–1149, doi:10.5194/cp-12-  
 775 1137-2016, 2016.

776 Thatcher, D. L., Wanamaker, A. D., Denniston, R. F., Asmerom, Y., Polyak, V. J., Fullick,  
 777 D., Ummenhofer, C. C., Gillikin, D. P. and Haws, J. A.: Hydroclimate variability from  
 778 western Iberia (Portugal) during the Holocene: Insights from a composite stalagmite isotope  
 779 record, *The Holocene*, 30(7), 966–981, doi:<https://doi.org/10.1177/0959683620908648>,  
 780 2020.

781 Trondman, A.-K., Gaillard, M.-J., Mazier, F., Sugita, S., Fyfe, R., Nielsen, A. B., Twiddle,  
 782 C., Barratt, P., Birks, H. J. B., Bjune, A. E., Björkman, L., Broström, A., Caseldine, C.,  
 783 David, R., Dodson, J., Dörfler, W., Fischer, E., van Geel, B., Giesecke, T., Hultberg, T.,  
 784 Kalnina, L., Kangur, M., van der Knaap, P., Koff, T., Kuneš, P., Lagerås, P., Latałowa, M.,  
 785 Lechterbeck, J., Leroyer, C., Leydet, M., Lindbladh, M., Marquer, L., Mitchell, F. J. G.,  
 786 Odgaard, B. V., Peglar, S. M., Persson, T., Poska, A., Rösch, M., Seppä, H., Veski, S. and  
 787 Wick, L.: Pollen-based quantitative reconstructions of Holocene regional vegetation cover  
 788 (plant-functional types and land-cover types) in Europe suitable for climate modelling, *Glob.*  
 789 *Chang. Biol.*, 21(2), 676–697, doi:<https://doi.org/10.1111/gcb.12737>, 2015.

790 Villegas-Diaz, Roberto; Cruz-Silva, Esmeralda; Harrison, S. P.: ageR: Supervised age  
 791 models, , doi:10.5281/zenodo.4636715, 2021.

792 Walczak, I. W., Baldini, J. U. L., Baldini, L. M., McDermott, F., Marsden, S., Standish, C.  
793 D., Richards, D. A., Andreo, B. and Slater, J.: Reconstructing high-resolution climate using  
794 CT scanning of unsectioned stalagmites: A case study identifying the mid-Holocene onset of  
795 the Mediterranean climate in southern Iberia, *Quat. Sci. Rev.*, 127, 117–128,  
796 doi:<https://doi.org/10.1016/j.quascirev.2015.06.013>, 2015.

797 Wei, D., González-Sampériz, P., Gil-Romera, G., Harrison, S. P. and Prentice, I. C.: Seasonal  
798 temperature and moisture changes in interior semi-arid Spain from the last interglacial to the  
799 Late Holocene, *Quat. Res.*, 101, 143–155, doi: 10.1017/qua.2020.108, 2021.

800 Wu, H., Guiot, J., Brewer, S. and Guo, Z.: Climatic changes in Eurasia and Africa at the last  
801 glacial maximum and mid-Holocene: reconstruction from pollen data using inverse  
802 vegetation modelling, *Clim. Dyn.*, 29(2), 211–229, doi:10.1007/s00382-007-0231-3, 2007.

803 Zapata, L., Peña-Chocarro, L., Pérez-Jordá, G. and Stika, H.-P.: Early Neolithic Agriculture  
804 in the Iberian Peninsula, *J. World Prehistory*, 18(4), 283–325, 2004.

805 Zhang, Y., Kong, Z., Ni, J., Yan, S. and Yang, Z.: Late Holocene palaeoenvironment change  
806 in central Tianshan of Xinjiang, northwest China, *Grana*, 46(3), 197–213,  
807 doi:10.1080/00173130701564748, 2007.

808

809 **Figure and Table Captions**

810 Figure 1. Climate space represented by mean temperature of the coldest month (MTCO),  
 811 mean temperature of the warmest month (MTWA), and plant-available moisture as  
 812 represented by  $\alpha$ , an estimate of the ratio of actual evapotranspiration to equilibrium  
 813 evapotranspiration. The grey points show climate values for a rectangular area ( $21^{\circ}$  W  $\sim$   $150^{\circ}$   
 814 E,  $29^{\circ}$  N  $\sim$   $82^{\circ}$  N) enclosing the SMPDS data set, derived from the Climate Research Unit  
 815 CRU CL 2.0 database (New et al., 2002). The black points show climate values of the  
 816 SMPDS dataset. The red points show climate values of the Iberian Peninsula region in the  
 817 SMPDS dataset.

818 Figure 2. Map showing the location of the 117 fossil sites in the Iberian Peninsula used for  
 819 climate reconstructions. Sites lower than 1000 m a.s.l. are shown as squares, sites higher than  
 820 1000 m a.s.l. are shown as triangles. The base maps show modern (a) mean temperature of  
 821 the coldest month (MTCO), (b) mean temperature of the warmest month (MTWA), and (c)  
 822 plant-available moisture as represented by  $\alpha$ , an estimate of the ratio of actual  
 823 evapotranspiration to equilibrium evapotranspiration.

824 Figure 3. Reconstructed anomalies in climate at individual sites through time. The sites are  
 825 grouped into high ( $>1000$ m) and low ( $<1000$ m) elevation sites and organised from west to east.  
 826 Grey cells indicate periods or longitudes with no data. The individual plots show the anomalies  
 827 in reconstructed (a,d) mean temperature of the coldest month (MTCO), (b,e) mean temperature  
 828 of the warmest month (MTWA), and (c,f) plant-available moisture as represented by  $\alpha$ , an  
 829 estimate of the ratio of actual evapotranspiration to equilibrium evapotranspiration. The  
 830 anomalies are expressed as deviations of the mean value in each bin ( $\pm 500$  years) from the  
 831 most recent bin ( $0.5$  ka  $\pm 500$  years) at each site.

832 Figure 4. Reconstructed composite changes (anomalies to 0.5 ka) in (a) mean temperature of  
 833 the coldest month (MTCO), (b) mean temperature of the warmest month (MTWA) and (c)  
 834 plant-available moisture as represented by  $\alpha$ , through the Holocene compared to changes in (d)  
 835 winter and (e) summer insolation for the latitude of the Iberian Peninsula, using  $\pm 500$  years as  
 836 the bin. The black lines show mean values across sites, with vertical line segments showing the  
 837 standard deviations of mean values using 1000 bootstrap cycles of site resampling.

838 Figure 5. Changes in the west-east gradient of plant-available moisture as represented by  
 839 anomalies in  $\alpha$  relative to 0.5 ka at individual sites through the Holocene. The red lines show  
 840 the regression lines. The shades indicate the 95 % confidence intervals of the regression lines

841 Figure 6. The relationship between mean temperature of the warmest month (MTWA) and  
 842 plant-available moisture as represented by  $\alpha$  (a) in the modern climate data set, and (b) in the  
 843 Holocene reconstructions.

844 Figure 7. Comparison between reconstructed composite changes in climate anomalies. The first  
 845 column represents this paper, the second column represents Mauri et al. (2015), the third  
 846 column represents Kaufman et al. (2020), the fourth column represents Tarroso et al. (2016).  
 847 The composite curves from this paper and Kaufman et al. (2020) are calculated from individual  
 848 reconstructions, using anomalies to 0.5 ka and a bin of  $\pm 500$  years (time slices are 0.5, 1.5, ...,  
 849 11.5 ka). The composite curves from Mauri et al. (2015) are converted directly from the gridded  
 850 time slices which are provided with anomalies to 0.1 ka and a bin of  $\pm 500$  years (time slices  
 851 are 1, 2, ..., 12 ka). The composite curves from Tarroso et al. (2016) are also converted directly  
 852 from the gridded time slices provided, with anomalies to 0.5 ka and a bin of  $\pm 500$  years (time  
 853 slices are 3, 4, ..., 12 ka). Note that Tarroso et al. (2016) applied a smoothing to the data such  
 854 that the plots in their paper do not show the excursion in MTWA at 8 ka. In all of the plots, the  
 855 black lines show mean values across sites, with vertical line bars showing the standard  
 856 deviation of mean values using 1000 bootstrap cycles of site/grid resampling.

857 Figure 8. Simulated mean values of mean temperature of the coldest month (MTCO), mean  
 858 temperature of the warmest month (MTWA) and mean daily precipitation in Iberian Peninsula  
 859 between 8 ka and 0 ka, smoothed using 100 year bins. Here BP means before 1950 AD. The  
 860 black lines represent Max Planck Institute Earth System Model (MPI) simulations, the red lines  
 861 represent Alfred Wagner Institute Earth System Model (AWI) simulations, the blue lines  
 862 represent Institut Pierre Simon Laplace Climate Model (IPSL-CM5) TR5AS simulations, the  
 863 gold lines represent Institut Pierre Simon Laplace Climate Model (IPSL-CM6) TR6AV  
 864 simulations. The four simulations were forced by evolving orbital parameters and greenhouse  
 865 gas concentrations. The four models have different spatial resolution, with the finest resolution  
 866 being  $1.875^\circ \times 1.875^\circ$  (AWI, MPI) and the coarsest resolution being  $1.875^\circ \times 3.75^\circ$  (IPSL-  
 867 CM5, TR5AS).

868 Table 1. Details of the fossil pollen sites used. The fossil pollen data from the Iberian  
 869 Peninsula were compiled by Shen et al. (2022) and obtained from  
 870 <https://doi.org/10.17864/1947.000343>. The reference list of this table can be found in the  
 871 supplementary.

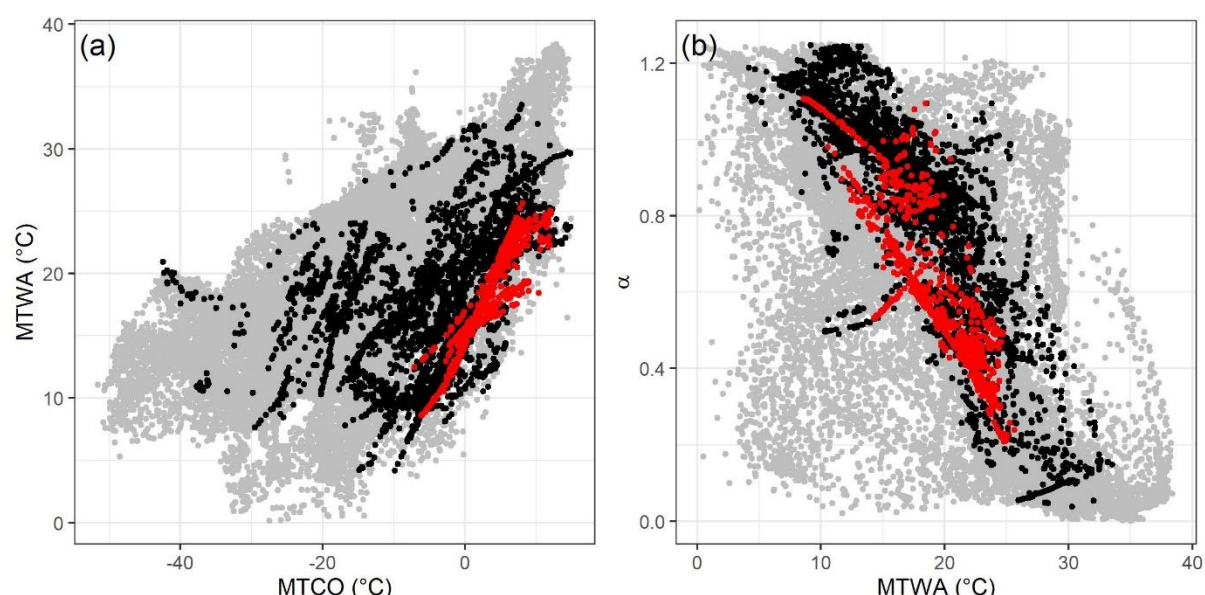
872 Table 2. Leave-out cross-validation (with geographically and climatically close sites  
 873 removed) fitness of the modified version of fxTWA-PLS, for mean temperature of the coldest  
 874 month (MTCO), mean temperature of the warmest month (MTWA) and plant-available  
 875 moisture ( $\alpha$ ), with p-spline smoothed fx estimation, using bins of 0.02, 0.02 and 0.002,  
 876 showing results for all the components. RMSEP is the root-mean-square error of prediction.  
 877  $\Delta$ RMSEP is the per cent change of RMSEP using the current number of components than  
 878 using one component less.  $p$  assesses whether using the current number of components is  
 879 significantly different from using one component less, which is used to choose the last

880 significant number of components (indicated in bold) to avoid over-fitting. The degree of  
881 overall compression is assessed by linear regression of the cross-validated reconstructions  
882 onto the climate variable,  $b1$ ,  $b1.se$  are the slope and the standard error of the slope,  
883 respectively. The closer the slope ( $b1$ ) is to 1, the less the overall compression is.

884 Table 3. Canonical Correspondence Analysis (CCA) result of modern and fossil-  
885 reconstructed MTCO, MTWA and  $\alpha$ . The summary statistics for the ANOVA-like  
886 permutation test (999 permutations) are also shown. VIF is the variance inflation factor, Df is  
887 the number of degrees of freedom,  $\chi^2$  is the constrained eigenvalue (or the sum of constrained  
888 eigenvalues for the whole model), F is significance, and Pr (>F) is the probability. The CCA  
889 plots can be found in the Supplementary (Fig. S11).

890 Table 4. Assessment of the significance of anomalies to 0.5 ka through time with longitude  
891 and elevation. The slope is obtained by linear regression of the anomaly onto the longitude or  
892 elevation.  $p$  is the significance of the slope (bold parts:  $p < 0.05$ ).  $x_0$  is the point where the  
893 anomaly is 0 in the linear equation, which indicates longitude or elevation where the anomaly  
894 changes sign.

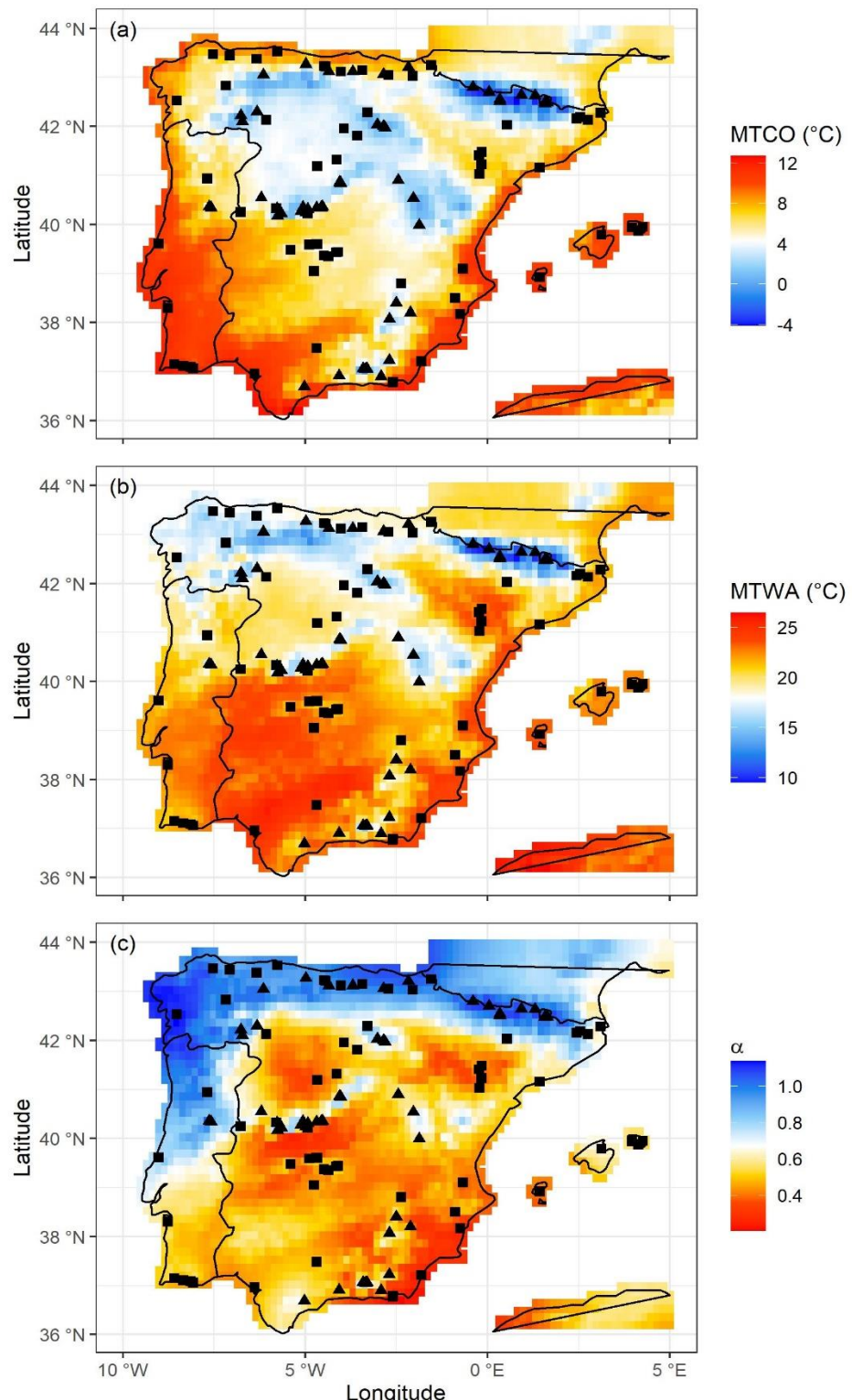
895 Figure 1. Climate space represented by mean temperature of the coldest month (MTCO),  
 896 mean temperature of the warmest month (MTWA), and plant-available moisture as  
 897 represented by  $\alpha$ , an estimate of the ratio of actual evapotranspiration to equilibrium  
 898 evapotranspiration. The grey points show climate values for a rectangular area ( $21^{\circ}$  W  $\sim$   $150^{\circ}$   
 899 E,  $29^{\circ}$  N  $\sim$   $82^{\circ}$  N) enclosing the SMPDS data set, derived from the Climate Research Unit  
 900 CRU CL 2.0 database (New et al., 2002). The black points show climate values of the  
 901 SMPDS dataset. The red points show climate values of the Iberian Peninsula region in the  
 902 SMPDS dataset.  
 903



904

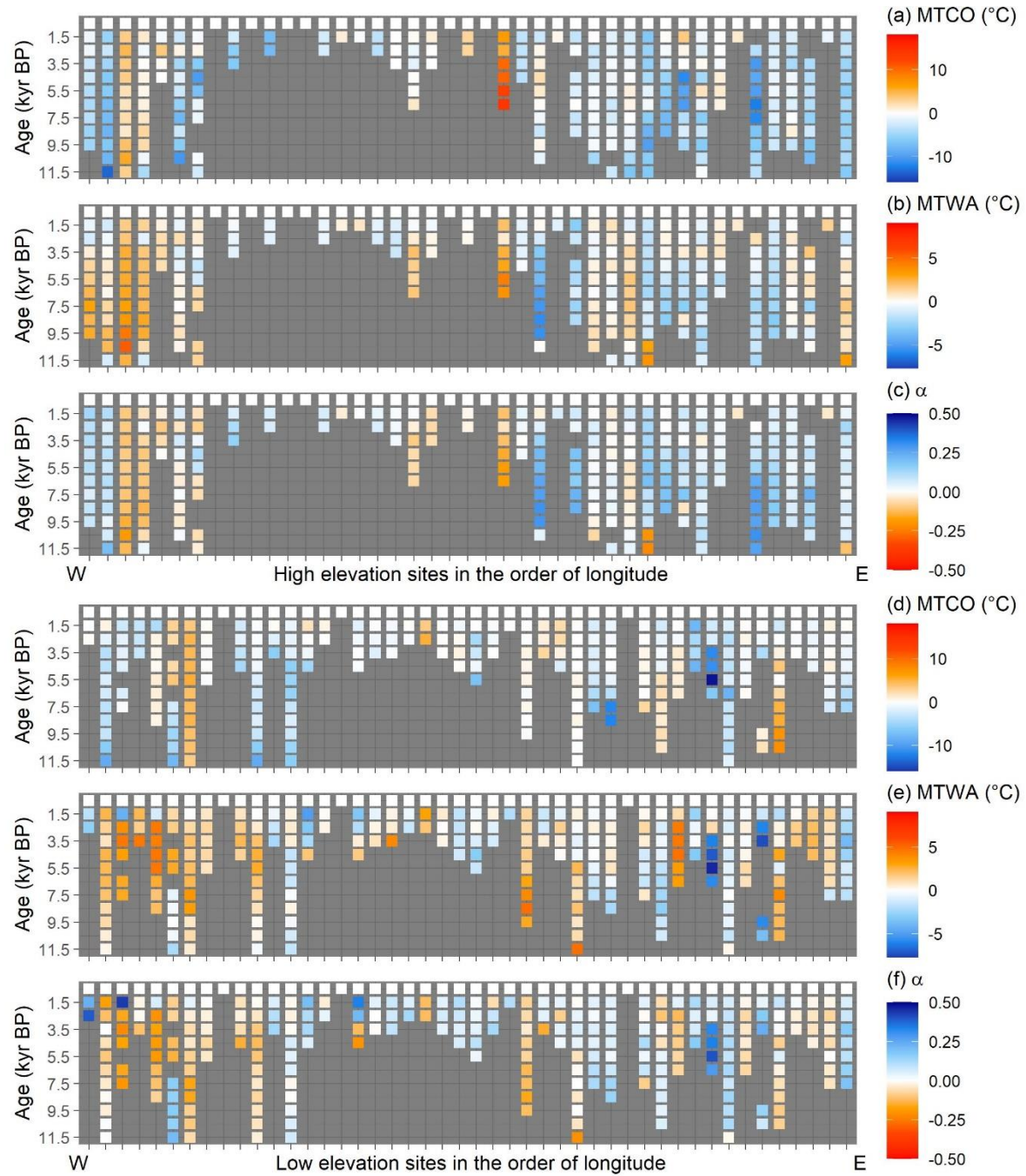
905 Figure 2. Map showing the location of the 117 fossil sites in the Iberian Peninsula used for  
 906 climate reconstructions. Sites lower than 1000 m a.s.l. are shown as squares, sites higher than  
 907 1000 m a.s.l. are shown as triangles. The base maps show modern (a) mean temperature of  
 908 the coldest month (MTCO), (b) mean temperature of the warmest month (MTWA), and (c)  
 909 plant-available moisture as represented by  $\alpha$ , an estimate of the ratio of actual  
 910 evapotranspiration to equilibrium evapotranspiration.

911

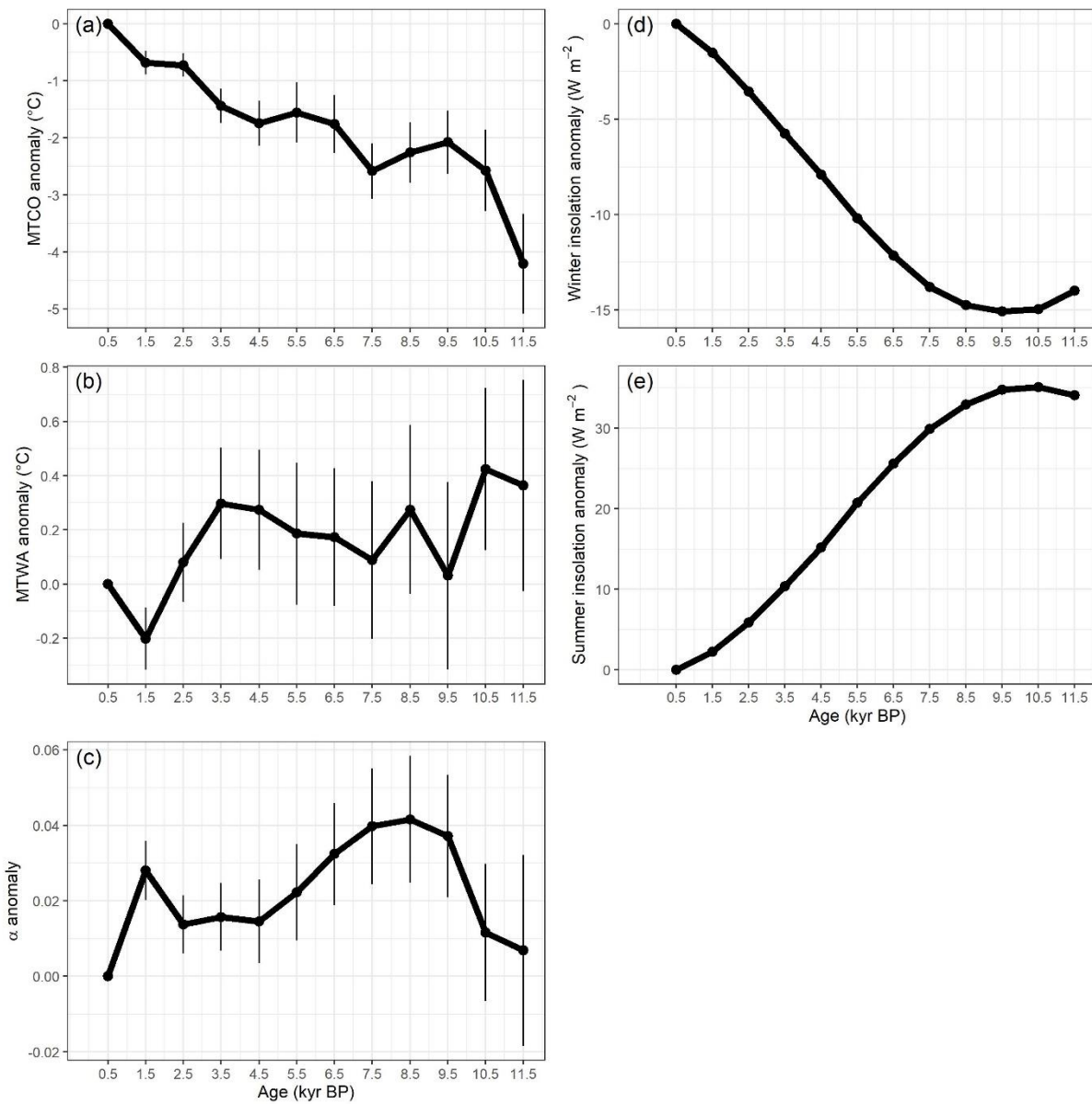


912

913 Figure 3. Reconstructed anomalies in climate at individual sites through time. The sites are  
 914 grouped into high (>1000m) and low (<1000m) elevation sites and organised from west to  
 915 east. Grey cells indicate periods or longitudes with no data. The individual plots show the  
 916 anomalies in reconstructed (a,d) mean temperature of the coldest month (MTCO), (b,e) mean  
 917 temperature of the warmest month (MTWA), and (c,f) plant-available moisture as  
 918 represented by  $\alpha$ , an estimate of the ratio of actual evapotranspiration to equilibrium  
 919 evapotranspiration. The anomalies are expressed as deviations of the mean value in each bin  
 920 ( $\pm 500$  years) from the most recent bin ( $0.5$  ka  $\pm 500$  years) at each site.  
 921

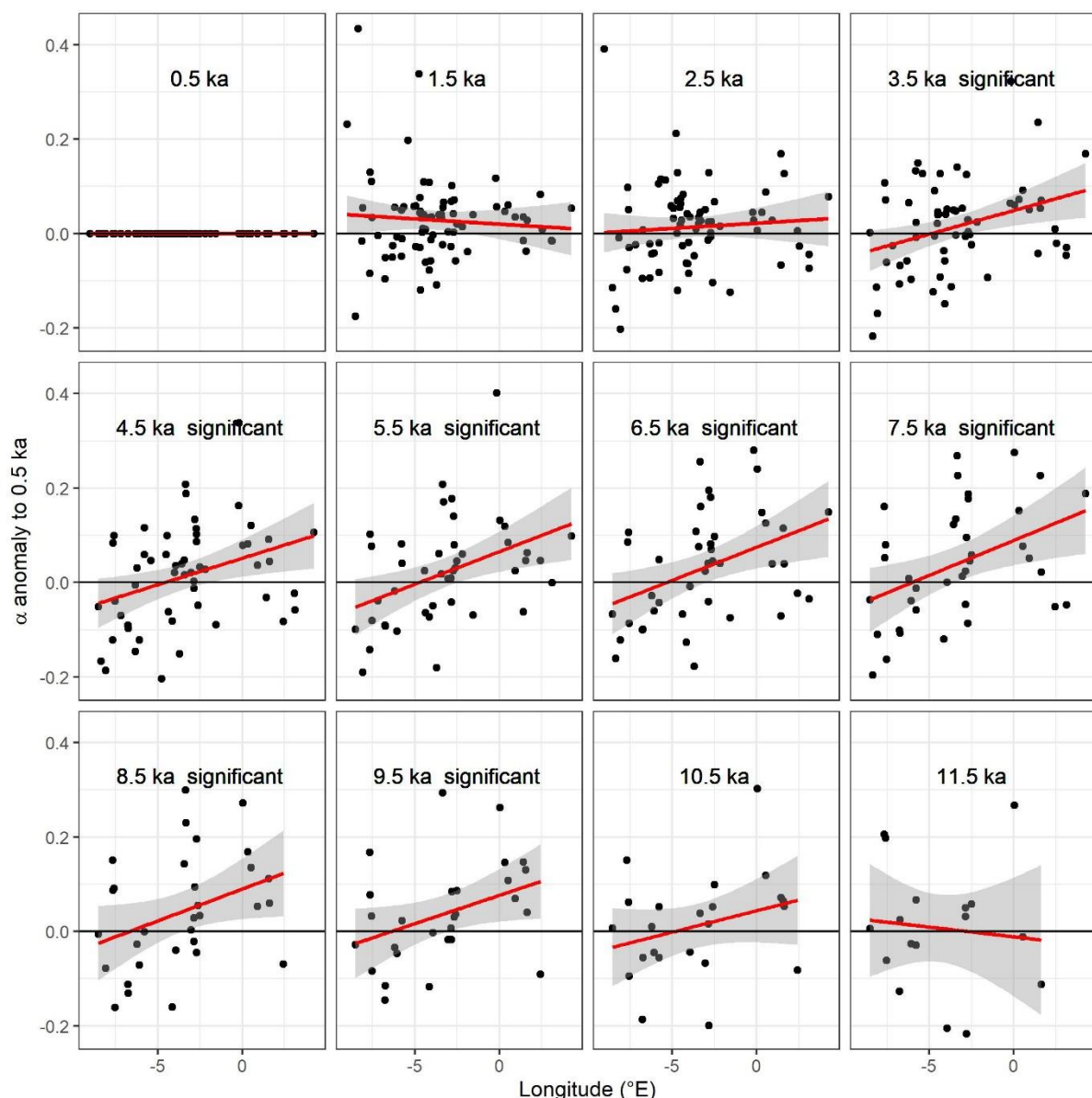


923 Figure 4. Reconstructed composite changes (anomalies to 0.5 ka) in (a) mean temperature of  
 924 the coldest month (MTCO), (b) mean temperature of the warmest month (MTWA) and (c)  
 925 plant-available moisture as represented by  $\alpha$ , through the Holocene compared to changes in  
 926 (d) winter and (e) summer insolation for the latitude of the Iberian Peninsula, using  $\pm 500$   
 927 years as the bin. The black lines show mean values across sites, with vertical line segments  
 928 showing the standard deviations of mean values using 1000 bootstrap cycles of site  
 929 resampling.  
 930



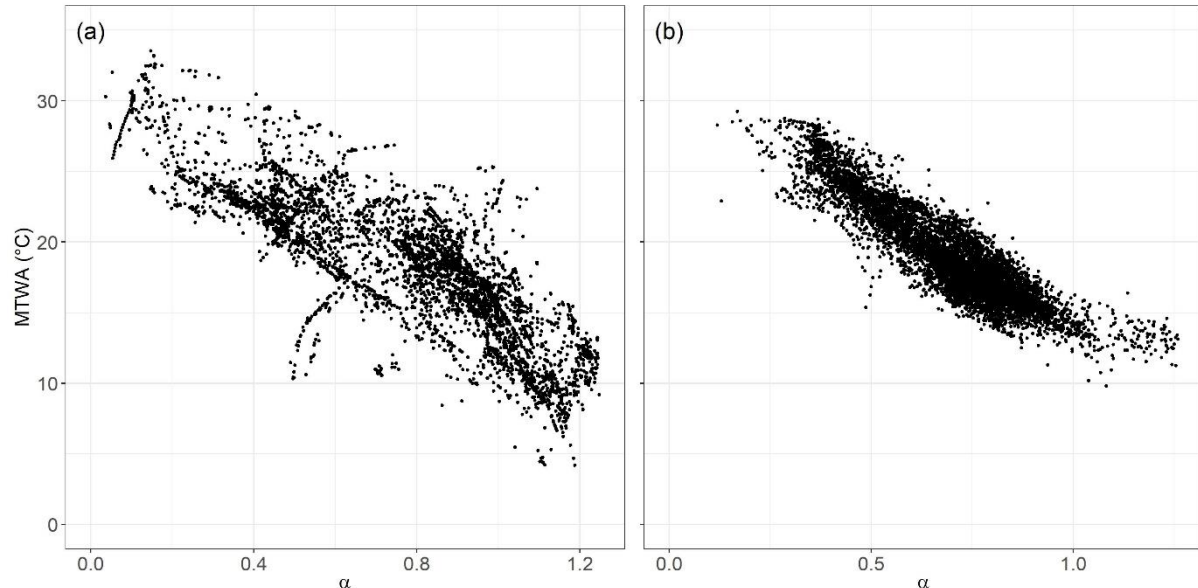
931

932 Figure 5. Changes in the west-east gradient of plant-available moisture as represented by  
 933 anomalies in  $\alpha$  relative to 0.5 ka at individual sites through the Holocene. The red lines show  
 934 the regression lines. The shades indicate the 95 % confidence intervals of the regression lines.  
 935



937 Figure 6. The relationship between mean temperature of the warmest month (MTWA) and  
938 plant-available moisture as represented by  $\alpha$  (a) in the modern climate data set, and (b) in the  
939 Holocene reconstructions.

940

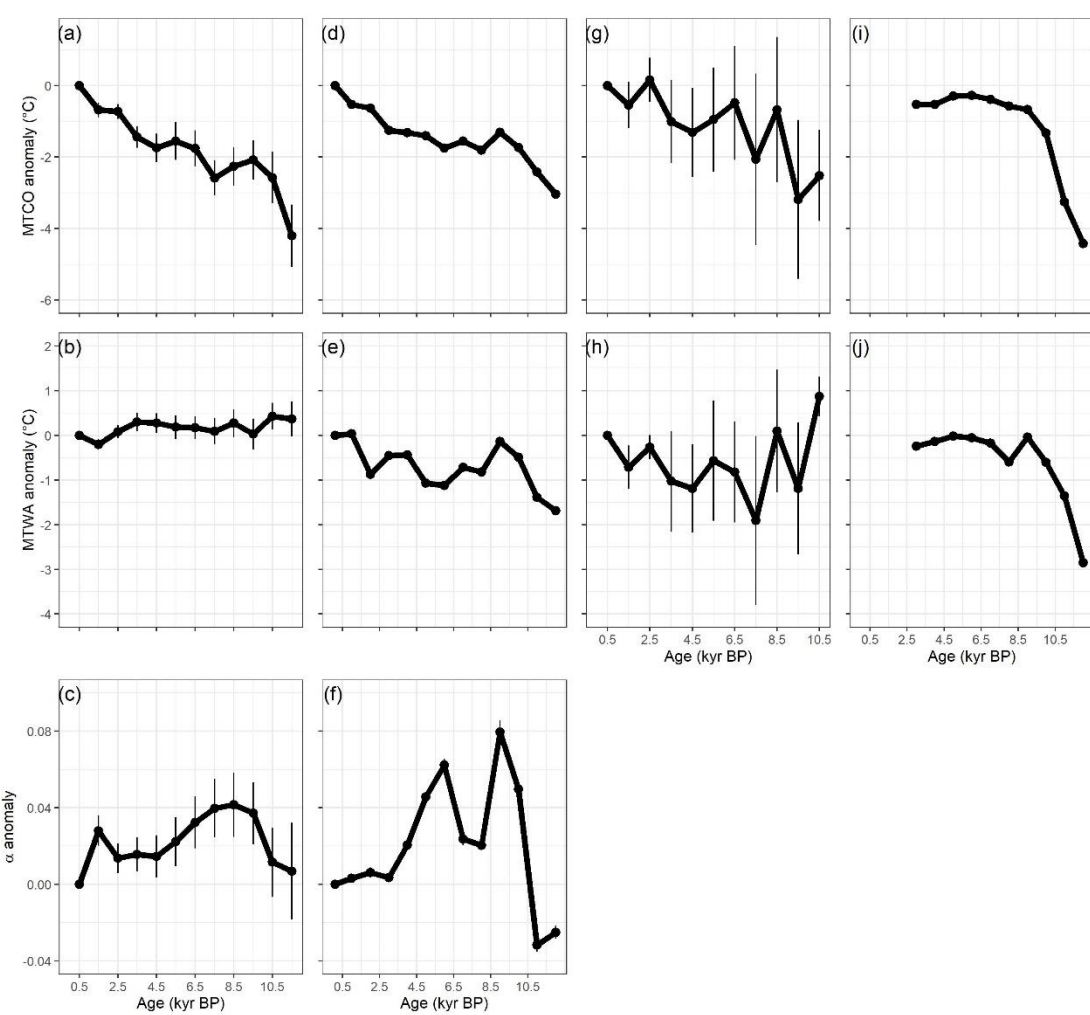


941

942

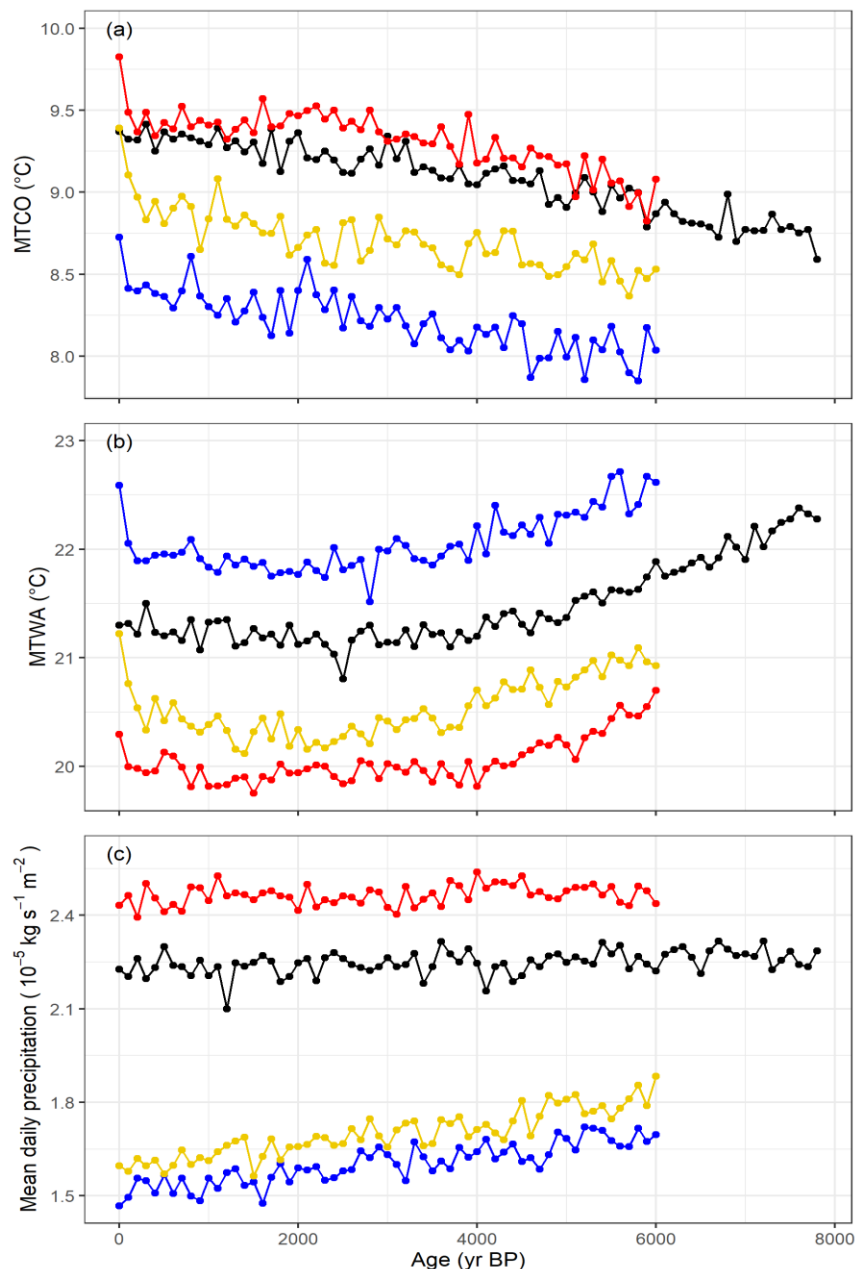
943

944 Figure 7. Comparison between reconstructed composite changes in climate anomalies. The first  
 945 column represents this paper, the second column represents Mauri et al. (2015), the third  
 946 column represents Kaufman et al. (2020), the fourth column represents Tarroso et al. (2016).  
 947 The composite curves from this paper and Kaufman et al. (2020) are calculated from individual  
 948 reconstructions, using anomalies to 0.5 ka and a bin of  $\pm 500$  years (time slices are 0.5, 1.5, ...,  
 949 11.5 ka). The composite curves from Mauri et al. (2015) are converted directly from the gridded  
 950 time slices which are provided with anomalies to 0.1 ka and a bin of  $\pm 500$  years (time slices  
 951 are 1, 2, ..., 12 ka). The composite curves from Tarroso et al. (2016) are also converted directly  
 952 from the gridded time slices provided, with anomalies to 0.5 ka and a bin of  $\pm 500$  years (time  
 953 slices are 3, 4, ..., 12 ka). Note that Tarroso et al. (2016) applied a smoothing to the data such  
 954 that the plots in their paper do not show the excursion in MTWA at 8 ka. In all of the plots, the  
 955 black lines show mean values across sites, with vertical line bars showing the standard  
 956 deviation of mean values using 1000 bootstrap cycles of site/grid resampling.  
 957



958  
 959

960 Figure 8. Simulated mean values of mean temperature of the coldest month (MTCO), mean  
 961 temperature of the warmest month (MTWA) and mean daily precipitation in Iberian  
 962 Peninsula between 8 ka and 0 ka, smoothed using 100 year bins. Here BP means before 1950  
 963 AD. The black lines represent Max Planck Institute Earth System Model (MPI) simulations,  
 964 the red lines represent Alfred Wagner Institute Earth System Model (AWI) simulations, the  
 965 blue lines represent Institut Pierre Simon Laplace Climate Model (IPSL-CM5) TR5AS  
 966 simulations, the gold lines represent Institut Pierre Simon Laplace Climate Model (IPSL-  
 967 CM6) TR6AV simulations. The four simulations were forced by evolving orbital parameters  
 968 and greenhouse gas concentrations. The four models have different spatial resolution, with  
 969 the finest resolution being  $1.875^\circ \times 1.875^\circ$  (AWI, MPI) and the coarsest resolution being  
 970  $1.875^\circ \times 3.75^\circ$  (IPSL-CM5, TR5AS).



972 Table 1. Details of the fossil pollen sites used. The fossil pollen data from the Iberian Peninsula were compiled by Shen et al. (2022) and obtained  
 973 from <https://doi.org/10.17864/1947.000343>. The reference list for this table can be found in the supplementary.

974

site name	entity name	longitude (°E)	latitude (°N)	elevation (m)	earliest sample (yr BP)	latest sample (yr BP)	length of record (yr)	no of samples	no of dating points	source	reference
Albufera Alcudia	ALCUDIA	3.12	39.79	0	7921	17	7904	54	4	EPD	Burjachs et al., (1994)
Algendar	ALGENDAR	3.96	39.94	21	8908	3816	5092	118	4	EPD	Yll et al., (1995, 1997)
Almenara de Adaja	ADAJA	-4.67	41.19	784	2830	477	2353	25	2	EPD	López Merino et al., (2009)
Alsa	ALSA	-4.02	43.12	560	4908	150	4758	24	3	EPD	Mariscal (1993)
Alvor Estuary Ribeira do Farelo Ribeira da Torre	Abi 05/07	-8.59	37.15	1	7840	1699	6141	76	9	author	Schneider et al., (2010, 2016)
Antas	ANTAS	-1.82	37.21	0	11141	4309	6832	95	6	EPD	Yll et al., (1995); Cano Villanueva, J. P. (1997); Pantaléon-Cano et al., (2003)
Arbarrain Mire	ARBARRAIN	-2.17	43.21	1004	6872	78	6794	91	8	author	Pérez-Díaz et al., (2018)
Armacao de Pera Ribeira de Alcantarilha	ADP 01/06	-8.34	37.11	2	7926	8	7918	17	7	author	Schneider et al., (2010, 2016)
Armena	Armena	0.34	42.51	2238	5668	2217	3451	53	27	author	Leunda et al., (2019)
Arroyo de Aguas Frias	AGUASFRIAS	-5.12	40.27	1120	196	-41	237	50	5	author	Julio Camarero et al., (2019)
Arroyo de las Cárcavas	CARCAVAS	-4.03	40.84	1300	2346	-57	2403	40	6	EPD	Morales-Molino et al., (2017a)
Arroyo de Navalacarreta	NAVALACA	-4.03	40.85	1250	706	-60	766	38	6	EPD	Morales-Molino et al., (2017a)
Arroyo de Valdeconejos	VALDECON	-4.06	40.86	1380	611	-56	667	44	8	EPD	Morales-Molino et al., (2017a)
Atxuri	ATXURI01	-1.55	43.25	500	6877	495	6382	33	2	EPD	Penalba (1994); Penalba and Garmendia (1989)
Ayoó de Vidriales	AYOO	-6.07	42.13	780	11846	-26	11872	63	15	EPD	Morales-Molino & García-Antón (2014)
Basa de la Mora	BSM08	0.33	42.55	1906	9856	184	9672	135	16	author	Pérez-Sanz et al., (2013)
Bassa Nera	BSN6	0.92	42.64	1891	9599	-55	9654	62	8	author	Garcés-Pastor et al., (2017)
Bermu Mire	BERMU	-4.15	39.43	783	1192	-25	1217	38	8	author	Luelmo-Lautenschlaeger et al., (2018a)
Borreguil de la Caldera	BdIC-01	-3.32	37.05	2992	1440	-56	1496	80	6	author	Ramos-Román et al., (2016)

Bosc dels Estanyons	BOSCESTA	1.63	42.48	2180	11761	26	11735	91	8	EPD	Miras et al., (2007); De Beaulieu et al., (2005)
Botija Bog	BOTIJA	-4.7	39.6	755	3773	82	3691	25	4	author	Luelmo-Lautenschlaeger et al., (2018b)
Cañada de la Cruz	CANCRUZ	-2.69	38.07	1595	9413	-6	9419	39	14	EPD	Yll et al., (1997)
Cala'n Porter	CPORTER	4.13	39.87	24	8809	4802	4007	86	4	EPD	Yll et al., (1994, 1995)
Cala Galdana	GALDANA	3.96	39.94	47	8498	4830	3668	101	5	EPD	López-Merino et al., (2012)
Campo Lameiro	PRD4	-8.52	42.53	260	11948	-11	11959	42	6	EPD	Carrión et al., (2007)
Canada del Gitano_Sierra de Baza	SBAZA	-2.7	37.23	1900	8460	103	8357	111	8	EPD	Cerrillo Cuenca et al., (2007); Cerrillo Cuenca & González Cordero (2011)
Canaleja	CANALEJA	-2.45	40.9	1029	11544	5515	6029	6	2	EPD	Carrión et al., (2001)
Castello Lagoon	Castello Lagoon core EM	3.1	42.28	2	4944	307	4637	85	10	author	Ejarque et al., (2016)
Cha das Lameiras	LAMEIRAS	-7.68	40.94	950	11982	539	11443	32	8	author	Burjachs & Expósito (2015)
Charco da Candieira	CANDIEIR	-7.58	40.34	1409	11970	32	11938	230	31	EPD	Mariscal Alvarez et al., (1983)
Creixell	CreixellT	1.43	41.16	1	6438	723	5715	32	2	EPD	López-Sáez et al., (2013)
Cueto de la Avellanosa	CUETOAV	-4.36	43.12	1320	6969	292	6677	34	3	EPD	López-Sáez et al., (2017)
Culazón	CULAZON	-4.49	43.23	592	3895	-44	3939	69	11	EPD	van der Knaap & van Leeuwen (1984, 1995, 1997)
El Brezosa	BREZOSA	-4.36	39.35	733	3958	-16	3974	68	11	author	Burjachs & Expósito (2015); Burjachs et al., (1997)
El Carrizal	CARRIZAL	-4.14	41.32	860	9851	0	9851	50	6	EPD	Morales-Molino et al., (2018)
El Maíllo mire	MAI	-6.21	40.55	1100	10687	91	10596	104	10	EPD	Franco-Múgica, et al., (2005)
El Payo	ELPAYO	-6.77	40.25	1000	571	-56	627	50	6	EPD	Morales-Molino et al., (2013)
El Perro mire	ELPERRO	-4.76	39.05	690	4694	-69	4763	41	10	author	Abel Schaad et al., (2009); Silva-Sánchez et al., (2016)
El Portalet	PORTALET	-0.4	42.8	1802	11838	2128	9710	207	13	author	Luelmo-Lautenschlaeger (2019a, 2019b)
El Redondo	REDONDO	-5.66	40.22	1765	3222	31	3191	60	4	author	González-Sampériz et al., (2006)
El Sabinar	SABINAR	-2.12	38.2	1117	6580	1140	5440	129	9	EPD	López-Sáez et al., (2016)
El Tiemblo	TIEMBLO	-4.53	40.36	1250	3184	3	3181	60	9	author	Carrión et al., (2004)
Elx	ELX	-0.75	38.17	1	9903	3392	6511	79	4	EPD	López-Sáez et al., (2018a)

Enol	ENOL	-4.99	43.27	1075	10910	2487	8423	30	7	author	Moreno et al., (2011)
Es Grau	ESGRAU	4.26	39.95	2	7648	-13	7661	98	15	EPD	Burjachs et al., (2017)
Espinosa de Cerrato	CERRATO	-3.94	41.96	885	11578	822	10756	157	7	author	Múgica et al., (2001); Morales-Molino et al., (2017b)
Estanilles	ESTANILLES	1.3	42.63	2247	11908	7646	4262	57	11	EPD	Pérez-Obiol et al., (2012)
Estanya	Estanya Catena	0.53	42.03	677	11882	-37	11919	48	21	author	González-Sampériz et al., (2017); Morellón et al., (2011)
Fuente de la Leche	LECHE	-5.06	40.35	1382	2783	-18	2801	58	10	author	Robles-López et al., (2018)
Fuente del Pino Blanco	PINOBLANCO	-4.98	40.24	1343	653	-38	691	96	5	author	Robles-López et al., (2018)
Hinojos Marsh	HINOJOS	-6.39	36.96	2	4737	2682	2055	46	5	author	López-Sáez et al., (2018b)
Hort Timoner	HTIMONER	4.13	39.88	40	8686	5089	3597	46	4	EPD	Yll et al., (1997)
Hoya del Castillo	N-CAS	-0.16	41.48	258	10740	5629	5111	34	3	EPD	Davis & Stevenson (2007)
La Cruz	LACRUZ	-1.87	39.99	1024	1521	12	1509	23	2	EPD	Burjachs (1996)
La Molina mire	MOLINAES	-6.33	43.38	650	4482	388	4094	152	6	author	López-Merino et al., (2011)
Labradillos Mire	LABRADILLOS	-4.57	40.34	1460	1447	184	1263	25	5	author	Robles López et al., (2017)
Lago de Ajo	LAGOAJO	-6.15	43.05	1570	11755	2175	9580	44	6	EPD	McKeever et al., (1984); Allen et al., (1996)
Lagoa Comprida 2	LAGOA_CO	-7.64	40.36	1650	9863	94	9769	68	4	EPD	Janssen & Woldringh (1981); Moe & Van Der Knaap (1990); Van Den Brink & Janssen (1985)
Lagoa Travessa	TRAVESS1	-8.77	38.3	3	8174	3617	4557	65	4	EPD	Mateus (1985); Mateus (1989)
Laguna de la Mosca	LdIMo composite	-3.31	37.06	2889	8344	-63	8407	68	18	author	Manzano et al., (2019)
Laguna de la Mula	LdIM 10-02	-3.42	37.06	2497	4581	-60	4641	32	8	author	Jiménez-Moreno et al., (2013)
Laguna de la Roya	LAROYA	-6.77	42.22	1608	11927	-41	11968	54	7	PANGAE A	Allen et al., (1996)
Laguna de Rio Seco	Laguna de Rio Seco core 1	-3.35	37.05	3020	10455	-54	10509	69	13	author	Anderson et al., (2011)
Laguna Guallar	N-GUA	-0.23	41.41	336	10654	8056	2598	30	6	EPD	Davis & Stevenson (2007)
Laguna Mesagosa	LAGMESAG	-2.81	41.97	1600	11981	-48	12029	90	5	EPD	Engelbrechten (1999)
Laguna Negra	LAGNEGRA	-2.85	42	1760	11253	-48	11301	68	9	EPD	Engelbrechten (1999)
Laguna Salada Chiprana	N-SAL	-0.17	41.23	150	6872	-40	6912	39	4	EPD	Valero-Garcés et al., (2000)

Lake Banyoles	BANYOLES_1, Banyoles SB2	2.75	42.13	174	11952	3316	8636	141	15	EPD	Pèrez-Obiol & Julià (1994); Revelles et al., (2015)
Lake Saloio	SALOIO	-9.02	39.61	70	2804	313	2491	24	2	EPD	Gomes (2011)
Lanzahíta	LANZBOG	-4.94	40.22	558	2657	-51	2708	51	8	author	López-Sáez et al., (1999, 2010)
Las Animas Mire	ANIMAS	-5.03	36.69	1403	797	-57	854	48	10	author	Alba-Sánchez et al., (2019)
Las Lanchas	LANCHAS	-4.89	39.59	800	374	-8	382	20	2	author	Luelmo-Lautenschlaeger et al., (2018c)
Las Pardillas	LASPARDI	-3.03	42.03	1850	10954	404	10550	74	4	EPD	Sanchez-Goñi & Hannon (1999)
Las Vinuelas	VINUELAS	-4.49	39.37	761	4210	-56	4266	58	9	author	Morales-Molino et al., (2019)
Les Palanques	PALANQUES	2.44	42.16	460	10011	524	9487	77	3	EPD	Revelles et al., (2018)
Manaderos	Manaderos core	-4.69	40.34	1292	1293	37	1256	59	9	author	Robles-López et al., (2020)
Marbore	Marbore composite	0.04	42.7	2612	11683	-18	11701	61	18	author	Leunda et al., (2017)
Monte Areo mire	AREO	-5.77	43.53	200	11547	-35	11582	55	12	EPD	López-Merino et al., (2010)
Montes do Buio Cuadramón	CUAII	-7.53	43.47	700	11347	241	11106	19	4	EPD	González et al., (2000)
Navamuno	Navamuno_S3	-5.78	40.32	1505	11971	-28	11999	207	12	author	López-Sáez et al., (2020)
Navarrés	NAVA1, NAVARRE3	-0.68	39.1	225	11104	3131	7973	72	15	EPD	Carrión & Dupre (1996); Carrión & Van Geel (1999)
Ojos del Tremendal	Ojos del Tremendal core 1	-2.04	40.54	1650	11875	1253	10622	52	4	author	Stevenson (2000)
Patateros bog	PATATERO	-4.67	39.6	700	2655	-19	2674	28	4	EPD	Dorado-Valiño et al., (2014)
Peña Negra	PENANEGR	-5.79	40.33	1000	3434	-62	3496	63	7	EPD	Stefanini (2008)
Pedrido	PEDRIDO	-7.07	43.44	770	5256	106	5150	71	30	EPD	Mighall et al., (2006)
Pena de Cadela	CADELA	-7.17	42.83	970	5233	-14	5247	91	9	EPD	Abel-Schaad & López-Sáez (2013)
Pico del Sertal	SERTAL	-4.44	43.22	940	5200	106	5094	9	3	EPD	Mariscal Alvarez (1986)
Pla de l'Estany	PLAESTANY	2.54	42.19	520	3577	-37	3614	43	4	EPD	Burjachs (1994)
Planell de Perafita	PERAFITA	1.57	42.48	2240	10244	-1	10245	56	11	EPD	Miras et al., (2010)
Posidonia Lligat	LLIGAT	-3.29	42.29	-3	779	15	764	32	5	EPD	López-Sáez et al., (2009)
Pozo de la Nieve	PozoN_2015 core	-4.55	40.35	1600	2258	-37	2295	41	10	author	Robles-López et al., (2017)

Prailllos de Bossier Mire	BOSSIER	-4.07	36.91	1610	3428	4	3424	25	3	EPD	Abel-Schaad et al., (2017)
Prat de Vila	PRATVILA	1.43	38.92	4	10776	538	10238	29	5	EPD	Burjachs et al., (2017)
Puerto de Belate	BELATE01	-2.05	43.03	847	8457	1746	6711	60	3	EPD	Penalba (1994); Penalba and Garmendia (1989)
Puerto de las Estaces de Trueba	ESTACAS	-3.7	43.12	1160	6263	391	5872	9	3	PANGAE A	Mariscal (1989)
Puerto de Los Tornos	TORNOS01	-3.43	43.15	920	8718	-34	8752	47	4	EPD	Penalba and Garmendia (1989)
Puerto de Serranillos	SERRANIL	-4.93	40.31	1700	2254	-50	2304	34	5	EPD	López-Merino et al., (2009)
Quintanar de la Sierra	QUINTA02	-3.02	42.03	1470	11995	1953	10042	37	20	EPD	Penalba (1994); Penalba and Garmendia (1989)
Roquetas de Mar	ROQUETAS	-2.59	36.79	0	6910	1057	5853	32	3	EPD	Yll et al., (1995); Cano Villanueva (1997); Pantaléon-Cano (2003); Pérez-Obiol (1994)
Salada Pequeña	N-PEQ	-0.22	41.03	357	4350	669	3681	43	5	EPD	Davis (2010)
Saldropo	SALDROPO	-2.72	43.05	625	7577	403	7174	76	3	EPD	Penalba (1994, 1989)
Salines playa-lake	SALINES	-0.89	38.5	475	11905	1394	10511	74	7	EPD	Burjachs et al., (2017)
San Rafael	SANRAFA	-2.6	36.77	0	10846	-30	10876	134	6	EPD	Cano Villanueva (1997); Pantaléon-Cano et al., (2003); Yll et al., (1995)
Sanabria Marsh	SANABRIA	-6.73	42.1	1050	11832	0	11832	79	9	EPD	Allen et al., (1996); Hannon (1985); Turner & Hannon (1988)
Serra Mitjana Fen	MITJANA	1.58	42.47	2406	1490	412	1078	15	2	EPD	Miras et al., (2015)
Serranía de las Villuercas	VILLUERCAS	-5.4	39.48	1000	4156	128	4028	31	4	author	Gil-Romera et al., (2008)
Sierra de Gádor	GADOR	-2.92	36.9	1530	6222	1195	5027	86	6	EPD	Carrión et al., (2003)
Siles Lake	SILES	-2.5	38.4	1320	11527	189	11338	67	12	EPD	Carrión (2002)
Tubilla del Lago	TUB	-3.57	41.81	900	7436	31	7405	88	13	EPD	Morales-Molino et al., (2017b)
Turbera de La Panera Cabras	PANERA	-5.76	40.17	1648	164	-56	220	23	2	EPD	Abel Schaad et al., (2009)
Valdeyernos bog	VALDEYER	-4.1	39.44	850	3160	-60	3220	25	4	EPD	Dorado-Valiño et al., (2014)
Valle do Lobo Ribeira de Carcavai	VdL PB2	-8.07	37.06	2	8331	16	8315	144	20	author	Schneider et al., (2010, 2016)
Verdeospesoa mire	VERDEOSPES OA	-2.86	43.06	1015	11137	0	11137	91	12	author	Pérez-Díaz & López-Sáez (2017)

Vilamora Ribeira de Quarteira	Vilamora P01-5	-8.14	37.09	4	3851	919	2932	30	12	author	Schneider et al., (2010, 2016)
Villaverde	VILLAVERDE	-2.37	38.8	870	8066	0	8066	104	9	EPD	Carrión et al., (2001)
Xan de Llamas	XL	-6.32	42.3	1500	4113	34	4079	33	4	EPD	Morales-Molino et al., (2011)
Zoñar	ZONARcombi ned	-4.69	37.48	300	3234	-45	3279	52	17	author	Martín-Puertas et al., (2008)

975

976 Table 2. Leave-out cross-validation (with geographically and climatically close sites  
 977 removed) fitness of the modified version of fxtWA-PLS, for mean temperature of the coldest  
 978 month (MTCO), mean temperature of the warmest month (MTWA) and plant-available  
 979 moisture ( $\alpha$ ), with p-spline smoothed fx estimation, using bins of 0.02, 0.02 and 0.002,  
 980 showing results for all the components. RMSEP is the root-mean-square error of prediction.  
 981  $\Delta$ RMSEP is the per cent change of RMSEP using the current number of components than  
 982 using one component less.  $p$  assesses whether using the current number of components is  
 983 significantly different from using one component less, which is used to choose the last  
 984 significant number of components (indicated in bold) to avoid over-fitting. The degree of  
 985 overall compression is assessed by linear regression of the cross-validated reconstructions  
 986 onto the climate variable,  $b_1$ ,  $b_1$ .se are the slope and the standard error of the slope,  
 987 respectively. The closer the slope ( $b_1$ ) is to 1, the less the overall compression is.  
 988  
 989

	ncomp	$R^2$	avg. bias	max. bias	min. bias	RMSEP	$\Delta$ RMSEP	$p$	$b_1$	$b_1$ .se
MTCO	1	0.70	-0.86	25.23	0.00	5.20	-39.97	0.001	0.89	0.01
	2	0.73	-0.73	25.00	0.00	4.87	-6.29	0.001	0.91	0.01
	3	0.74	-0.71	24.38	0.00	4.86	-0.32	0.001	0.91	0.01
	<b>4</b>	<b>0.75</b>	<b>-0.59</b>	<b>24.27</b>	<b>0.00</b>	<b>4.70</b>	<b>-3.26</b>	<b>0.001</b>	<b>0.91</b>	<b>0.01</b>
	5	0.74	-0.63	34.54	0.00	4.77	1.51	1.000	0.91	0.01
MTWA	1	0.52	-0.29	17.13	0.00	3.72	-26.88	0.001	0.69	0.01
	2	0.56	-0.14	17.20	0.00	3.53	-5.06	0.001	0.71	0.01
	3	0.56	-0.13	17.01	0.00	3.53	-0.20	0.008	0.71	0.01
	<b>4</b>	<b>0.57</b>	<b>-0.11</b>	<b>17.30</b>	<b>0.00</b>	<b>3.47</b>	<b>-1.56</b>	<b>0.001</b>	<b>0.71</b>	<b>0.01</b>
	5	0.57	-0.11	17.34	0.00	3.48	0.10	0.780	0.71	0.01
$\alpha$	1	0.65	-0.014	0.787	0.000	0.165	-39.59	0.001	0.76	0.01
	2	0.68	-0.016	0.781	0.000	0.159	-3.55	0.001	0.77	0.01
	<b>3</b>	<b>0.68</b>	<b>-0.017</b>	<b>0.757</b>	<b>0.000</b>	<b>0.158</b>	<b>-0.61</b>	<b>0.023</b>	<b>0.78</b>	<b>0.01</b>
	4	0.69	-0.017	0.784	0.000	0.158	-0.43	0.108	0.79	0.01
	5	0.69	-0.017	0.850	0.000	0.158	0.26	0.985	0.80	0.01

990

991 Table 3. Canonical Correspondence Analysis (CCA) result of modern and fossil-  
 992 reconstructed MTCO, MTWA and  $\alpha$ . The summary statistics for the ANOVA-like  
 993 permutation test (999 permutations) are also shown. VIF is the variance inflation factor, Df is  
 994 the number of degrees of freedom,  $\chi^2$  is the constrained eigenvalue (or the sum of constrained  
 995 eigenvalues for the whole model), F is significance, and Pr (>F) is the probability. The CCA  
 996 plots can be found in the Supplementary (Fig. S11).  
 997

	<b>Axes</b>	<b>Axis 1</b>	<b>Axis 2</b>	<b>Axis 3</b>	<b>VIF</b>
	Constrained eigenvalues	0.3819	0.1623	0.1087	/
<b>Correlations of the environmental variables with the axes:</b>					
	MTCO	-0.815	0.579	0.012	1.31
	MTWA	-0.700	-0.203	0.685	3.34
	$\alpha$	0.883	0.430	-0.187	3.39
	<b>Df</b>	<b><math>\chi^2</math></b>	<b>F</b>	<b>Pr (&gt;F)</b>	
Modern	Whole model	3	0.6530	78.113	0.001
	MTCO	1	0.3082	110.597	0.001
	MTWA	1	0.1602	57.489	0.001
	$\alpha$	1	0.1846	66.252	0.001
	CCA 1	1	0.3819	137.076	0.001
	CCA 2	1	0.1623	58.252	0.001
	CCA 3	1	0.1087	39.011	0.001
	<b>Axes</b>	<b>Axis 1</b>	<b>Axis 2</b>	<b>Axis 3</b>	<b>VIF</b>
Fossil-reconstructed	Constrained eigenvalues	0.3601	0.2266	0.2037	/
<b>Correlations of the environmental variables with the axes:</b>					
	MTCO	0.430	0.776	0.462	1.34
	MTWA	0.987	0.141	-0.076	5.40
	$\alpha$	-0.947	0.088	-0.308	5.28
	<b>Df</b>	<b><math>\chi^2</math></b>	<b>F</b>	<b>Pr (&gt;F)</b>	
	Whole model	3	0.7905	226.98	0.001
	MTCO	1	0.2465	212.34	0.001
	MTWA	1	0.3298	284.07	0.001
	$\alpha$	1	0.2142	184.53	0.001
	CCA 1	1	0.3601	310.19	0.001
	CCA 2	1	0.2266	195.24	0.001
	CCA 3	1	0.2037	175.51	0.001

999 Table 4. Assessment of the significance of anomalies to 0.5 ka through time with longitude  
1000 and elevation. The slope is obtained by linear regression of the anomaly onto the longitude or  
1001 elevation.  $p$  is the significance of the slope (bold parts:  $p < 0.05$ ).  $x_0$  is the point where the  
1002 anomaly is 0 in the linear equation, which indicates longitude or elevation where the anomaly  
1003 changes sign.

1004

		Longitude (°E)				Elevation (km)		
		age (ka)	slope	$p$	$x_0$	slope	$p$	$x_0$
MTCO (°C)	0.5	0.00	/	/	0.00	/	/	
	1.5	-0.07	0.411	-13.02	-0.30	0.411	-1.21	
	2.5	-0.15	0.095	-8.56	-0.52	0.179	-0.40	
	3.5	-0.13	0.314	-14.83	-0.81	0.142	-0.77	
	4.5	-0.12	0.444	-17.28	-0.69	0.319	-1.46	
	5.5	-0.24	0.247	-9.49	-0.61	0.503	-1.43	
	6.5	-0.18	0.372	-12.74	-0.87	0.293	-0.88	
	7.5	-0.15	0.421	-20.39	-1.38	0.080	-0.67	
	8.5	-0.03	0.890	-77.87	-1.58	0.065	-0.10	
	9.5	0.01	0.954	156.31	-1.79	0.060	0.11	
	10.5	0.20	0.474	9.25	-1.38	0.241	-0.64	
	11.5	0.23	0.528	13.77	0.12	0.947	36.35	
MTWA (°C)	0.5	0.00	/	/	0.00	/	/	
	1.5	-0.01	0.862	-26.38	-0.05	0.830	-3.35	
	2.5	-0.09	0.137	-2.80	-0.45	0.092	1.19	
	3.5	<b>-0.23</b>	<b>0.005</b>	<b>-2.03</b>	-0.40	0.284	1.74	
	4.5	<b>-0.21</b>	<b>0.016</b>	<b>-2.01</b>	-0.58	0.126	1.55	
	5.5	<b>-0.26</b>	<b>0.011</b>	<b>-2.43</b>	-0.49	0.280	1.53	
	6.5	<b>-0.24</b>	<b>0.017</b>	<b>-2.30</b>	-0.62	0.137	1.41	
	7.5	<b>-0.26</b>	<b>0.012</b>	<b>-3.02</b>	<b>-1.05</b>	<b>0.019</b>	<b>1.28</b>	
	8.5	-0.24	0.061	-2.43	<b>-1.15</b>	<b>0.023</b>	<b>1.57</b>	
	9.5	<b>-0.32</b>	<b>0.013</b>	<b>-3.20</b>	-0.44	0.459	1.34	
	10.5	-0.18	0.115	-1.23	0.54	0.276	0.44	
	11.5	0.13	0.453	-7.25	0.37	0.663	0.22	
$\alpha$	0.5	0.00	/	/	0.00	/	/	
	1.5	0.00	0.508	8.99	-0.01	0.393	3.40	
	2.5	0.00	0.517	-9.89	0.02	0.249	0.19	
	3.5	<b>0.01</b>	<b>0.006</b>	<b>-4.91</b>	0.02	0.191	0.28	
	4.5	<b>0.01</b>	<b>0.010</b>	<b>-4.60</b>	<b>0.05</b>	<b>0.008</b>	<b>0.79</b>	
	5.5	<b>0.01</b>	<b>0.005</b>	<b>-4.75</b>	<b>0.05</b>	<b>0.027</b>	<b>0.67</b>	
	6.5	<b>0.01</b>	<b>0.007</b>	<b>-5.34</b>	<b>0.06</b>	<b>0.004</b>	<b>0.60</b>	
	7.5	<b>0.02</b>	<b>0.009</b>	<b>-6.05</b>	<b>0.09</b>	<b>0.000</b>	<b>0.75</b>	
	8.5	<b>0.01</b>	<b>0.049</b>	<b>-6.67</b>	<b>0.09</b>	<b>0.000</b>	<b>0.88</b>	
	9.5	<b>0.01</b>	<b>0.048</b>	<b>-6.40</b>	<b>0.07</b>	<b>0.012</b>	<b>0.70</b>	
	10.5	0.01	0.183	-4.85	0.02	0.535	0.59	
	11.5	0.00	0.713	-2.76	0.03	0.654	0.93	

1005

1006 **Appendix A**

1007 **Theoretical basis:**

1008 **The previous version of fxTWA-PLS (fxTWA-PLS1):**

1009 The estimated optimum ( $\hat{u}_k$ ) and unbiased tolerance ( $\hat{t}_k$ ) of each taxon are calculated from  
 1010 the modern training data set as follows:

$$1011 \quad \hat{u}_k = \frac{\sum_{i=1}^n y_{ik} x_i}{\sum_{i=1}^n y_{ik}} \quad (A1)$$

$$1012 \quad \hat{t}_k = \sqrt{\frac{\sum_{i=1}^n y_{ik} (x_i - \hat{u}_k)^2}{(1 - 1/N_{2k}) \sum_{i=1}^n y_{ik}}} \quad (A2)$$

1013 where

$$1014 \quad N_{2k} = \frac{1}{\sum_{i=1}^n \left( \frac{y_{ik}}{\sum_{i'=1}^n y_{i'k}} \right)^2} \quad (A3)$$

1015 where  $n$  is the total number of sites;  $y_{ik}$  is the observed abundance of the  $k^{th}$  taxon at the  $i^{th}$   
 1016 site;  $x_i$  is the observed climate value at the  $i^{th}$  site;  $N_{2k}$  is the effective number of occurrences  
 1017 for the  $k^{th}$  taxon.

1018 fx correction is applied as weight in the form of  $1/fx^2$  at regression at step 7 in Table 1 in Liu  
 1019 et al. (2020). The regression step uses robust linear model fitting by the R code:

$$1021 \quad rlm(x_i \sim comp_1 + comp_2 + \dots + comp_{pls}, weights = 1/fx^2) \quad (A4)$$

1022

1023 **The modified version of fxTWA-PLS (fxTWA-PLS2):**

1024 The distribution of  $y_{ik}$  is influenced by the distribution of the climate variable, so we need to  
 1025 apply the fx correction when calculating optimum and tolerance for each taxon as follows:

$$1026 \quad \hat{u}_k = \frac{\sum_{i=1}^n \frac{y_{ik} x_i}{f_{x_i}}}{\sum_{i=1}^n \frac{y_{ik}}{f_{x_i}}} \quad (A5)$$

$$1027 \quad \hat{t}_k = \sqrt{\frac{\sum_{i=1}^n \frac{y_{ik} (x_i - \hat{u}_k)^2}{f_{x_i}}}{\left(1 - \frac{1}{N_{2k}}\right) \sum_{i=1}^n \frac{y_{ik}}{f_{x_i}}}} \quad (A6)$$

1028 where

$$1029 \quad N_{2k} = \frac{1}{\sum_{i=1}^n \left( \frac{\frac{y_{ik}}{f_{x_i}}}{\sum_{i'=1}^n \frac{y_{i'k}}{f_{x_{i'}}}} \right)^2} \quad (A7)$$

1030 The modified version of fxTWA-PLS applies fx correction separately at taxon calculation  
 1031 and regression (step 2 and 7 in Table 1 in Liu et al., 2020), both using weight in the form of  
 1032  $1/fx$ . The regression step (step 7) then becomes:

1033  $rlm(x_i \sim comp_1 + comp_2 + \dots + comp_{pls}, weights = 1/fx)$  (A8)

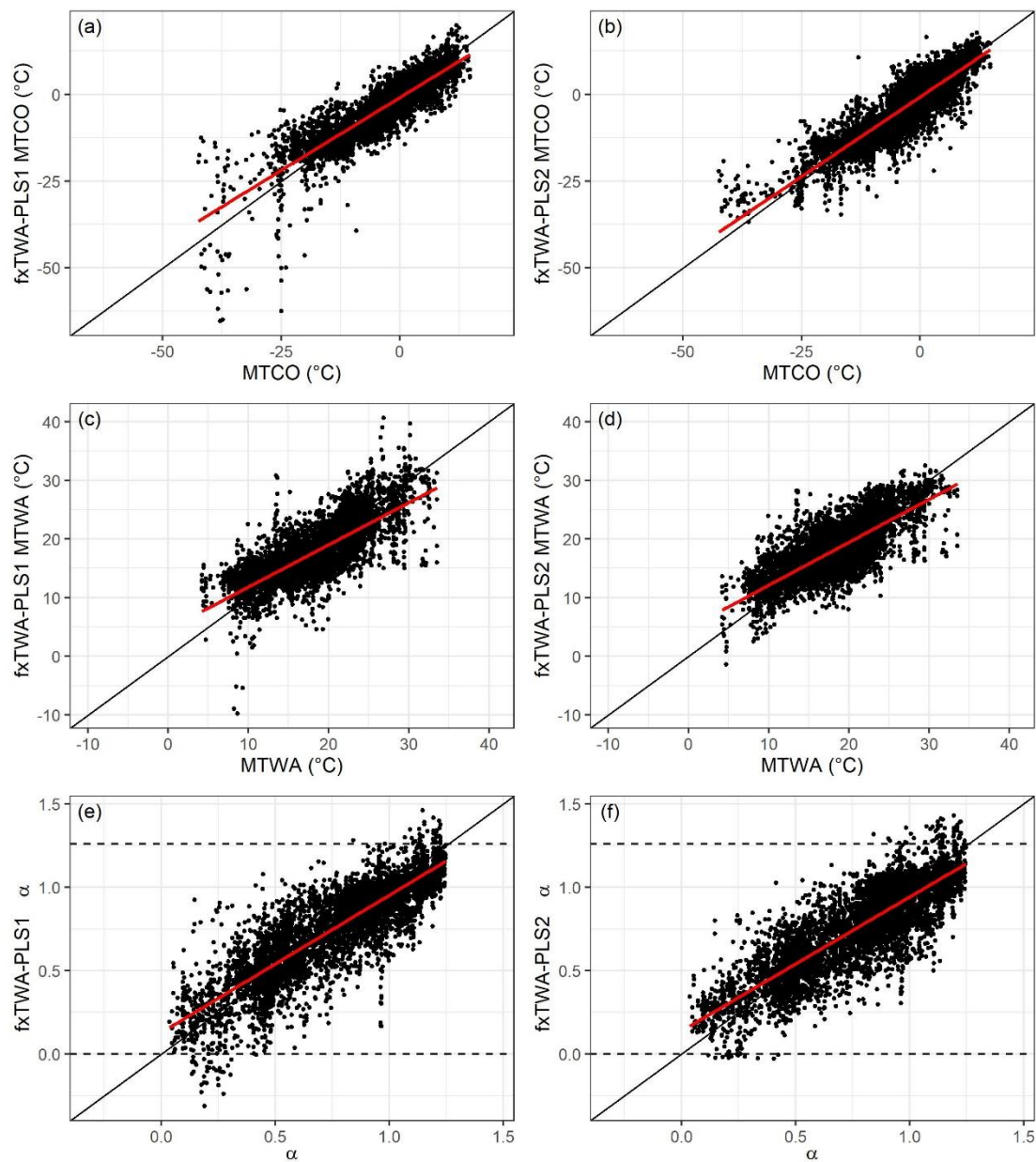
1034 The previous version uses fx values extracted from histograms, and different bin widths may  
1035 result in different training results. The modified version applies P-splines histogram  
1036 smoothing (Eilers and Marx, 2021) with third order difference penalty, which makes the fx  
1037 values almost independent of the bin width. The optimal smoothing parameter of the P-spline  
1038 penalty was determined by the HFS (Harville-Fellner-Schall) algorithm (Eilers and Marx,  
1039 2021) for the Poisson likelihood for the histogram counts.

1040 Table A1. Leave-out cross-validation (with geographically and climatically close sites removed)  
 1041 fitness of the previous and modified version of fxTWA-PLS (fxTWA-PLS1 and fxTWA-PLS2,  
 1042 respectively), for mean temperature of the coldest month (MTCO), mean temperature of the warmest  
 1043 month (MTWA) and plant-available moisture ( $\alpha$ ), using bins of 0.02, 0.02 and 0.002, respectively. n  
 1044 is the number of components used. RMSEP is the root mean square error of prediction.  $\Delta$ RMSEP is  
 1045 the per cent change of RMSEP using the current number of components than using one component  
 1046 less.  $p$  assesses whether using the current number of components is significantly different from using  
 1047 one component less, which is used to choose the last significant number of components (indicated in  
 1048 bold) to avoid overfitting. The degree of overall compression is assessed by doing linear regression to  
 1049 the cross-validation result and the climate variable.  $b_1$ ,  $b_1.se$  are the slope and the standard error of the  
 1050 slope, respectively. The closer the slope ( $b_1$ ) is to 1, the lower the overall compression is. fx  
 1051 correction is set intrinsic in functions in fxTWAPLS package for both versions in this paper, instead  
 1052 of relying on an outside input in Liu et al. (2020), so the values of fxTWA-PLS1 might be slighted  
 1053 different from values in Table 3 in Liu et al. (2020), but it doesn't affect the conclusion.  
 1054

	Method	n	$R^2$	avg. bias	max. bias	min. bias	RMSEP	$\Delta$ RMSEP	$p$	$b_1$	$b_1.se$
MTCO	fxTWA-PLS1	1	0.66	-0.86	31.17	0.00	5.21	-39.87	0.001	0.76	0.01
		2	0.72	-0.52	36.65	0.00	4.70	-9.78	0.001	0.80	0.01
		3	0.73	-0.47	41.18	0.00	4.62	-1.63	0.001	0.82	0.01
		<b>4</b>	<b>0.73</b>	<b>-0.51</b>	<b>44.86</b>	<b>0.00</b>	<b>4.58</b>	<b>-1.01</b>	<b>0.006</b>	<b>0.82</b>	<b>0.01</b>
		5	0.73	-0.41	58.35	0.00	4.62	0.89	0.708	0.83	0.01
	fxTWA-PLS2	1	0.70	-0.86	25.23	0.00	5.20	-39.97	0.001	0.89	0.01
		2	0.73	-0.73	25.00	0.00	4.87	-6.29	0.001	0.91	0.01
		3	0.74	-0.71	24.38	0.00	4.86	-0.32	0.001	0.91	0.01
		<b>4</b>	<b>0.75</b>	<b>-0.59</b>	<b>24.27</b>	<b>0.00</b>	<b>4.70</b>	<b>-3.26</b>	<b>0.001</b>	<b>0.91</b>	<b>0.01</b>
		5	0.74	-0.63	34.54	0.00	4.77	1.51	1.000	0.91	0.01
MTWA	fxTWA-PLS1	1	0.50	-0.53	17.91	0.00	3.87	-24.09	0.001	0.67	0.01
		<b>2</b>	<b>0.56</b>	<b>-0.54</b>	<b>17.71</b>	<b>0.00</b>	<b>3.52</b>	<b>-8.98</b>	<b>0.001</b>	<b>0.69</b>	<b>0.01</b>
		3	0.57	-0.49	25.14	0.00	3.52	0.09	0.565	0.73	0.01
		4	0.57	-0.43	34.92	0.00	3.56	1.12	0.974	0.75	0.01
		5	0.57	-0.46	32.23	0.00	3.55	-0.23	0.139	0.74	0.01
	fxTWA-PLS2	1	0.52	-0.29	17.13	0.00	3.72	-26.88	0.001	0.69	0.01
		2	0.56	-0.14	17.20	0.00	3.53	-5.06	0.001	0.71	0.01
		3	0.56	-0.13	17.01	0.00	3.53	-0.20	0.008	0.71	0.01
		<b>4</b>	<b>0.57</b>	<b>-0.11</b>	<b>17.30</b>	<b>0.00</b>	<b>3.47</b>	<b>-1.56</b>	<b>0.001</b>	<b>0.71</b>	<b>0.01</b>
		5	0.57	-0.11	17.34	0.00	3.48	0.10	0.780	0.71	0.01
$\alpha$	fxTWA-PLS1	1	0.63	-0.020	0.773	0.000	0.174	-36.23	0.001	0.78	0.01
		2	0.69	-0.012	0.902	0.000	0.157	-9.66	0.001	0.79	0.01
		<b>3</b>	<b>0.69</b>	<b>-0.011</b>	<b>0.820</b>	<b>0.000</b>	<b>0.155</b>	<b>-1.28</b>	<b>0.001</b>	<b>0.79</b>	<b>0.01</b>
		4	0.70	-0.010	0.786	0.000	0.156	0.25	0.867	0.81	0.01
		5	0.70	-0.010	0.786	0.000	0.156	0.09	1.000	0.81	0.01
	fxTWA-PLS2	1	0.65	-0.014	0.787	0.000	0.165	-39.59	0.001	0.76	0.01
		2	0.68	-0.016	0.781	0.000	0.159	-3.55	0.001	0.77	0.01
		<b>3</b>	<b>0.68</b>	<b>-0.017</b>	<b>0.757</b>	<b>0.000</b>	<b>0.158</b>	<b>-0.61</b>	<b>0.023</b>	<b>0.78</b>	<b>0.01</b>
		4	0.69	-0.017	0.784	0.000	0.158	-0.43	0.108	0.79	0.01
		5	0.69	-0.017	0.850	0.000	0.158	0.26	0.985	0.80	0.01

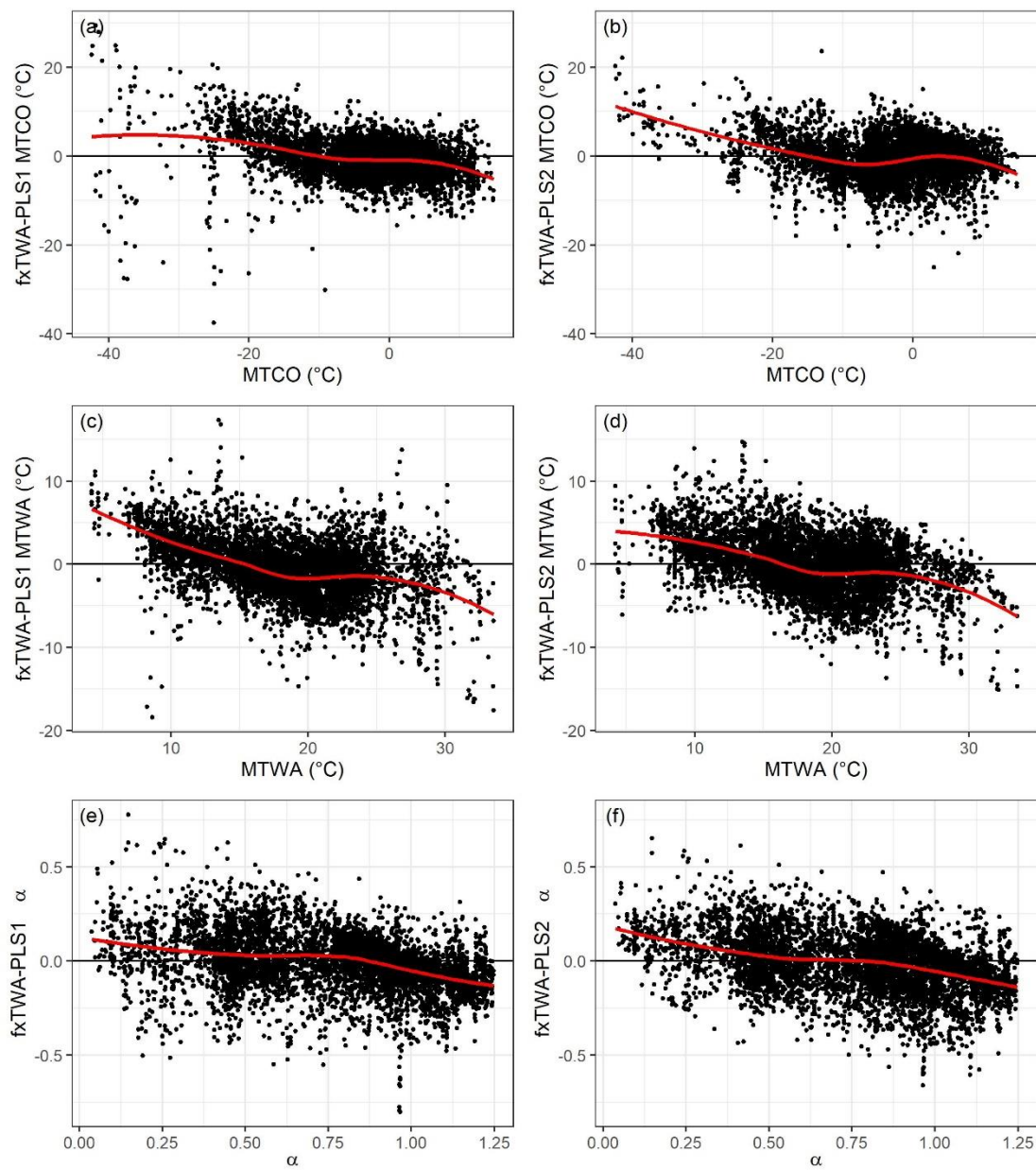
1055  
 1056

1057 Figure A1. Training results using the last significant number of components. The left panel  
 1058 shows the previous version (fxTWA-PLS1) and the right panel shows the modified version of  
 1059 fxTWA-PLS (fxTWA-PLS2). The 1: 1 line is shown in black; the linear regression line is  
 1060 shown in red, to show the degree of overall compression. The horizontal dashed lines indicate  
 1061 the natural limit of  $\alpha$  (0~1.26).  
 1062



1063  
 1064

1065 Figure A2. Residuals using the last significant number of components. The left panel shows  
 1066 the previous version (fxTWA-PLS1) and the right panel shows the modified version (fxTWA-  
 1067 PLS2) of fxTWA-PLS. The zero line is shown in black; the locally estimated scatterplot  
 1068 smoothing is shown in red, to show the degree of local compression.  
 1069



1070

1071